

RAPIDLY ROTATING SUNS AND ACTIVE NESTS OF CONVECTION

BENJAMIN P. BROWN

JILA and Dept. Astrophysical & Planetary Sciences, University of Colorado, Boulder, CO 80309-0440

MATTHEW K. BROWNING¹

Dept. of Astronomy, University of California, Berkeley, CA 94720-3411

ALLAN SACHA BRUN

DSM/IRFU/SAP, CEA-Saclay & UMR AIM, CEA-CNRS-Université Paris 7, 91191 Gif-sur-Yvette, France

MARK S. MIESCH

High Altitude Observatory, NCAR, Boulder, CO 80307-3000

AND

JURI TOOMRE

JILA and Dept. Astrophysical & Planetary Sciences, University of Colorado, Boulder, CO 80309-0440

(Received April 30, 2008; Revised July 1, 2008; Accepted August 12, 2008)

Submitted to ApJ

ABSTRACT

In the solar convection zone, rotation couples with intensely turbulent convection to drive a strong differential rotation and achieve complex magnetic dynamo action. Our sun must have rotated more rapidly in its past, as is suggested by observations of many rapidly rotating young solar-type stars. Here we explore the effects of more rapid rotation on the global-scale patterns of convection in such stars and the flows of differential rotation and meridional circulation which are self-consistently established. The convection in these systems is richly time dependent and in our most rapidly rotating suns a striking pattern of localized convection emerges. Convection near the equator in these systems is dominated by one or two nests in longitude of locally enhanced convection, with quiescent streaming flow in between at the highest rotation rates. These active nests of convection maintain a strong differential rotation despite their small size. The structure of differential rotation is similar in all of our more rapidly rotating suns, with fast equators and slower poles. We find that the total shear in differential rotation $\Delta\Omega$ grows with more rapid rotation while the relative shear $\Delta\Omega/\Omega_0$ decreases. In contrast, at more rapid rotation the meridional circulations decrease in energy and peak velocities and break into multiple cells of circulation in both radius and latitude.

Subject headings: convection – Sun:interior – Sun:rotation – stars:interiors – stars:rotation

1. CONVECTION, ROTATION AND MAGNETISM

Our sun is a magnetic star whose cycles of magnetic activity must arise from organized dynamo action in its interior. This dynamo action is achieved by turbulent plasma motions in the solar convection zone, which spans the outer 29% of the sun in radius. Here vigorous convective motions and rotation couple to drive the differential rotation and meridional circulation. These global-scale flows are important ingredients in stellar dynamo theory, providing shear which may build and organize fields on global scales. When our sun was younger, it must have rotated much more rapidly, as is suggested both by the solar wind which continually removes angular momentum from the sun and by many observations of rapidly rotating solar-like stars. In more rapidly rotating suns the coupling between rotation and convection is strong and must continue to drive global scales of flow. Understanding the nature of convection, differential rotation and meridional circulation in more rapidly rotating stars is a crucial step towards understanding stellar dynamos.

The manner in which the sun achieves global-scale dynamo action is gradually being sorted out. Helioseismology, which uses acoustic oscillations to probe the radial structure of the star as well as the convective flows beneath the surface, has revealed that the solar differential rotation profile observed at the surface prints throughout the convection zone with two prominent regions of radial shear. The near-surface shear layer occupies the outer 5% of the sun, whereas a tachocline of shear at the base of the convection zone separates the strong differential rotation of that zone from the uniform rotation of the deeper radiative interior (e.g., Thompson et al. 2003). The solar global magnetic dynamo, responsible for the 22-year cycles of activity, is now believed to be seated in that tachocline. In such interface dynamo models, magnetic fields generated in the bulk of the convection zone are pumped into the tachocline where the radial shear builds strong toroidal magnetic fields, with magnetic buoyancy leading to loops that rise upward and erupt through the solar surface (e.g., Charbonneau 2005; Miesch 2005). The differential rotation plays an important role in building and organizing the global-scale fields while the meridional circulations may be important for returning flux to the base of the convection zone and advecting it equatorward, enabling cycles of magnetic activ-

Electronic address: bpbrown@solarz.colorado.edu

¹present address: Dept of Astronomy & Astrophysics, U. Chicago, 5640 S. Ellis Ave, Chicago, IL 60637

ity. By studying the coupling of rotation and convection over a range of conditions, we are likely to learn about the operation of the current solar dynamo and about the nature of dynamos operating in our sun's past and in other solar-like stars.

Observations of young solar-like stars indicate that they rotate as much as 50 times faster than the current solar rate. Many of these more rapidly rotating stars possess strong magnetic fields. A correlation between rotation and magnetic activity is observed over a range of stellar types and populations, indicating that more rapidly rotating stars may have stronger stellar dynamos (e.g., Noyes et al. 1984; Patten & Simon 1996). Probing the nature of these dynamos and the impact of faster rotation on the internal stellar dynamics requires both accurate observations and detailed dynamical models of the stellar interiors. The faster flows of differential rotation are much easier to detect than the relatively slow motions associated with meridional circulations; observations across the HR diagram indicate that differential rotation is a common feature in many stars. Asteroseismic observations with the Kepler and Corot missions may soon begin to constrain the internal rotation structure. At present only measurements of surface differential rotation are available, as assessed with a variety of techniques including photometric variability (Donahue et al. 1996; Walker et al. 2007), Doppler imaging (Donati et al. 2003) and Fourier transform methods (Reiners & Schmitt 2003).

Advances in supercomputing have enabled 3-D simulations that are beginning to capture many of the dynamical elements of the solar convection zone. Early global-scale simulations of solar convection by Gilman (1975, 1977, 1979) under the Boussinesq approximation were extended by the pioneering work of Gilman & Glatzmaier (1981). Such global-scale simulations of solar convection conducted in full spherical shells sought to capture the largest scales of convective flows and began to study how they can establish differential rotation and meridional circulations. However, the range of spatial and temporal scales present in solar convection are vast and thus the computational resources required by the modeling are daunting. Through recent advances in massively parallel computer architectures, solar convection simulations are now beginning to make detailed contact with the observational constraints provided by helioseismology (e.g., Brun & Toomre 2002; Miesch et al. 2006, 2008). Other efforts have focused on the vigorous turbulence and the dynamo action achieved in the bulk of the solar convection zone (Brun et al. 2004), with recent studies beginning to include the tachocline as a region of penetrative overshoot, shear, and magnetic field amplification (Browning et al. 2006). Facilitated by these computational advances, models of convection and dynamo action within the cores of A-type stars have also begun to be investigated (Browning et al. 2004; Brun et al. 2005; Featherstone et al. 2007).

To date, most models of stellar differential rotation in stars like our sun that rotate more rapidly have been carried out in 2-D under the simplifying assumptions of mean field theory (e.g., Rüdiger et al. 1998; Küker & Stix 2001; Küker & Rüdiger 2005a,b). The time is ripe to pursue the question with fully 3-D simulations of global-scale stellar convection.

In order to study solar-like stars that rotate faster, our previous work focused on a series of 3-D compressible simulations within a spherical shell using the anelastic spherical harmonic (ASH) code for stars rotating from one to five times the current solar rate (Brown et al. 2004). These preliminary

hydrodynamic simulations explored how stellar convection changes with more rapid rotation, including the differential rotation and meridional circulation that is achieved. Comparable studies have been carried out by Ballot et al. (2007) studying younger stars with deeper convection zones. In our simulations we found that remarkable nests of vigorous convection emerge in the equatorial regions. Namely, convective structures at low latitudes about the equator can exhibit strong spatial modulation with longitude, and at high rotation rates the convection is confined to narrow intervals (or nests) in longitude. In the more turbulent simulations presented in this paper, which span a larger range of rotation rates from one to ten times the current solar rate, the phenomena of modulated convection has persisted and the active nests of convection are prominent features at the higher rotation rates. These nests of localized convection persist for long intervals of time and despite their small filling factor maintain a strong differential rotation.

The emergence of spatially localized convective states has been observed in other systems, particularly in theoretical studies of doubly-diffusive systems such as thermosolutal convection (e.g., Spina et al. 1998; Batiste et al. 2006), in laboratory studies of convection in binary fluids (e.g., Surko et al. 1991), and in simulations of magnetoconvection where isolated “convectons” have been observed (Blanchflower 1999). In shells of rapidly rotating fluid, temporally intermittent patches of localized convection emerged in Boussinesq simulations of the geodynamo (Grote & Busse 2000). In many of these systems, spatial modulation occurs in the weakly nonlinear regime close to the onset of convection. In contrast, our simulations of solar convection are in a regime of fully developed turbulent convection.

We describe briefly in §2 the 3-D anelastic spherical shell model and the parameter space explored by our simulations. In §3 we discuss the nature of convection realized in more rapidly rotating stars and the emergence of spatially-localized patterns of convection. In §§4-6 we examine the global-scale flows realized in our simulations, including differential rotation and meridional circulation, and their scaling with more rapid rotation. A detailed exploration of the active nests of convection is presented in §7. We reflect in §8 on the significance of our findings.

2. TOOLS TO MODEL 3-D STELLAR CONVECTION

To study through simulations the global scales of motion likely achieved in stellar convection zones, we must employ a global model which simultaneously captures the spherical shell geometry and admits the possibility of zonal jets and large eddy vortices, and of convective plumes that may span the depth of the convection zone. The solar convection zone is intensely turbulent and molecular values of viscosity and thermal diffusivity in the sun are estimated to be very small. As a consequence, numerical simulations cannot hope to resolve all scales of motion present in real solar convection and a compromise must be struck between resolving the important dynamics within small regions and capturing the connectivity and geometry of the global scales. We opt here for the latter by studying a full shell of convection.

2.1. Anelastic Simulation Approach

Our tool for exploring stellar convection is the anelastic spherical harmonic (ASH) code, which is described in detail in Clune et al. (1999) and in Brun et al. (2004). ASH

is designed to run efficiently on massively parallel architectures. ASH solves the three-dimensional (3-D) anelastic equations of motion in a rotating spherical shell using the pseudo-spectral method. The thermodynamic variations and the three components of mass flux are expanded in spherical harmonics to resolve their horizontal structure and in Chebyshev polynomials to resolve their radial structure. The anelastic approximation is used to capture the effects of density stratification without having to resolve sound waves which have short periods (about 5 minutes) relative to the dynamical time scales of most interest (months to years). The mass flux remains divergence-free by using a poloidal-toroidal representation. Temporal discretization is accomplished using a semi-implicit Crank-Nicholson time-stepping scheme for linear terms and an explicit Adams-Bashforth scheme for nonlinear terms. Under the anelastic approximation the thermodynamic variables are linearized about their spherically symmetric and evolving mean state with density $\bar{\rho}$, pressure \bar{P} , temperature \bar{T} and specific entropy \bar{S} . Fluctuations about this state are denoted as ρ , P , T and S respectively. In the uniformly rotating reference frame of the star, the resulting hydrodynamic equations expressing the conservation of mass, momentum and internal energy are in turn:

$$\nabla \cdot (\bar{\rho} \vec{v}) = 0, \quad (1)$$

$$\bar{\rho} \left[\frac{\partial \vec{v}}{\partial t} + (\vec{v} \cdot \nabla) \vec{v} + 2\vec{\Omega}_0 \times \vec{v} \right] = -\nabla(\bar{P} + P) + (\bar{\rho} + \rho) \vec{g} - \nabla \cdot \mathcal{D}, \quad (2)$$

$$\bar{\rho} \bar{T} \frac{\partial S}{\partial t} = \nabla \cdot \left[\kappa_r \bar{\rho} c_p \nabla(\bar{T} + T) + \kappa_0 \bar{\rho} \bar{T} \nabla \bar{S} + \kappa \bar{\rho} \bar{T} \nabla S \right] - \bar{\rho} \bar{T} \vec{v} \cdot \nabla(\bar{S} + S) + 2\bar{\rho} \nu \left[e_{ij} e_{ij} - \frac{1}{3}(\nabla \cdot \vec{v})^2 \right], \quad (3)$$

where $\vec{v} = (v_r, v_\theta, v_\phi)$ is the local velocity in the rotating frame of constant angular velocity $\vec{\Omega}_0$, \vec{g} is the gravitational acceleration, c_p is the specific heat at constant pressure, κ_r is the radiative diffusivity and \mathcal{D} is the viscous stress tensor, given by

$$\mathcal{D}_{ij} = -2\bar{\rho} \nu \left[e_{ij} - \frac{1}{3}(\nabla \cdot \vec{v}) \delta_{ij} \right], \quad (4)$$

where e_{ij} is the strain rate tensor. Here ν and κ are the diffusivities for vorticity and entropy. We assume an ideal gas law

$$\bar{P} = \mathcal{R} \bar{\rho} \bar{T}, \quad (5)$$

where \mathcal{R} is the gas constant, and close this set of equations using the linearized relations for the thermodynamic fluctuations

$$\frac{\rho}{\bar{\rho}} = \frac{P}{\bar{P}} - \frac{T}{\bar{T}} = \frac{P}{\gamma \bar{P}} - \frac{S}{c_p}. \quad (6)$$

The mean state variables are evolved with the fluctuations, thus allowing the convection to modify the entropy gradients which drive it.

ASH is a large-eddy simulation (LES) code, with subgrid-scale (SGS) treatments for scales of motion which fall below the spatial resolution in our simulations. We treat these scales with effective eddy diffusivities, ν and κ , which represent momentum and heat transport by unresolved motions in the simulations. Here for simplicity ν and κ are taken as functions of radius alone, and proportional to $\bar{\rho}^{-1/2}$. These simulations are similar to case AB as reported in Brun & Toomre

(2002) though with a different SGS functional form (there $\nu, \kappa \propto \bar{\rho}^{-1}$), and we shall consider faster Ω_0 . Our adopted SGS variation here, as in Brun et al. (2004), Browning et al. (2006) and Ballot et al. (2007), yields lower diffusivities near the top of the layer and thus higher Reynolds numbers. The thermal diffusion acting on the mean entropy gradient κ_0 is treated separately and occupies a narrow region in the upper convection zone. Its purpose is to transport heat through the outer surface where radial convective motions vanish.

Our simulations are still separated by many orders of magnitude from the intensely turbulent conditions present within the solar convection zone. They are likely to capture many aspects of the dynamics of solar convection, and we are encouraged by the success that similar simulations (e.g., Miesch et al. 2000; Brun & Toomre 2002; Miesch et al. 2006, 2008) have had in beginning to match the detailed observational constraints for differential rotation within the solar convection zone provided by helioseismology (c.f. Thompson et al. 2003).

We shall impose velocity boundary conditions which impose no net torques on the shell. These are in turn:

1. Impenetrable top and bottom: $v_r = 0$,
2. Stress-free top and bottom: $(\partial/\partial r)(v_\theta/r) = (\partial/\partial r)(v_\phi/r) = 0$, (7)
3. Constant entropy gradient at top and bottom: $\partial \bar{S}/\partial r = \text{const}$.

Some of our simulations are initialized by perturbing a quiescent state in solid body rotation. The growth of convection leads to velocity correlations that serve to redistribute angular momentum within the shell, building a differential rotation and meridional circulation. We evolve the simulation for long periods compared variously to convective overturning times, rotation periods or typical diffusive times. Other simulations were started from these evolved states and then run for long epochs after all adjustments have been made to the frame rotation rate Ω_0 and to the viscous and thermal diffusivities.

2.2. Studies of Global-Scale Convection in G-type Stars

Our numerical model is a relatively simple description of the solar convection zone that captures the essential spherical geometry and global connectivity of that domain. Solar values are taken for heat flux, mass and radius and a perfect gas is assumed. Near the solar surface the H and He ionization zones, coupled with radiative losses, drive intense convective motions on very small scales which appear at the surface as granulation. Capturing granulation in a global simulation would require spherical harmonic degrees of order 4000 and this is currently too demanding. We therefore position the top of our domain slightly below these ionization layers. In these simulations we also omit the stably stratified radiative interior and the shear layer at the base of the convection zone known as the tachocline. We focus here on the bulk of the convection zone, with our computational domain extending from $0.72R_\odot$ to $0.96R_\odot$, thus spanning 172 Mm in radius. The reference or mean state of our thermodynamic variables is derived from a one-dimensional solar structure model (Brun et al. 2002) and is continuously updated with the spherically symmetric components of the thermodynamic fluctuations as the simulations proceed. These values are illustrated in Figure 1 after convection has readjusted the stratification.

TABLE 1
 PARAMETERS FOR PRIMARY SIMULATIONS

Case	N_r, N_θ, N_ϕ	Ra	Ta	Re	Re'	Ro	Roc	ν	κ	Ω_0/Ω_\odot
G1	$96 \times 256 \times 512$	3.22×10^4	3.14×10^5	84	63	0.92	0.61	2.75	11.0	1
G2	$96 \times 256 \times 512$	1.75×10^5	3.21×10^6	205	85	0.55	0.45	1.72	6.87	2
G3	$96 \times 256 \times 512$	4.22×10^5	1.22×10^7	326	103	0.41	0.36	1.32	5.28	3
G4	$96 \times 256 \times 512$	7.89×10^5	3.18×10^7	433	119	0.33	0.31	1.09	4.36	4
G5	$96 \times 256 \times 512$	1.29×10^6	6.70×10^7	543	133	0.28	0.27	0.94	3.76	5
G7	$192 \times 512 \times 1024$	2.63×10^6	2.06×10^8	763	154	0.22	0.22	0.75	3.01	7
G10	$192 \times 512 \times 1024$	5.58×10^6	6.74×10^8	1051	188	0.17	0.18	0.59	2.37	10
G3a	$96 \times 256 \times 512$	7.83×10^5	2.41×10^7	528	158	0.50	0.34	0.94	3.76	3
G3b	$192 \times 256 \times 512$	2.26×10^6	8.02×10^7	1121	324	0.70	0.32	0.52	2.06	3
G5b	$192 \times 512 \times 1024$	4.03×10^6	2.23×10^8	1347	274	0.41	0.26	0.52	2.06	5

NOTE. — All simulations have inner radius $r_{\text{bot}} = 5.0 \times 10^{10}$ cm and outer radius of $r_{\text{top}} = 6.72 \times 10^{10}$ cm, with $L = (r_{\text{top}} - r_{\text{bot}}) = 1.72 \times 10^{10}$ cm the thickness of the spherical shell. Evaluated at mid-depth are the Rayleigh number $\text{Ra} = (-\partial\rho/\partial S)(d\bar{S}/dr)gL^4/\rho\nu\kappa$, the Taylor number $\text{Ta} = 4\Omega_0^2 L^4/\nu^2$, the rms Reynolds number $\text{Re} = v_{\text{rms}}L/\nu$ and fluctuating Reynolds number $\text{Re}' = v'_{\text{rms}}L/\nu$, the Rossby number $\text{Ro} = \omega/2\Omega_0$, and the convective Rossby number $\text{Roc} = (\text{Ra}/\text{TaPr})^{1/2}$. Here the fluctuating velocity v' has the differential rotation removed: $v' = v - \langle v \rangle$, with angle brackets denoting an average in longitude. The Prandtl number $\text{Pr} = \nu/\kappa$ is 0.25 for all simulations. The viscous and thermal diffusivity, ν and κ , are quoted at mid-depth (in units of 10^{12} cm²s⁻¹). The rotation rate of each reference frame Ω_0 is in multiples of $\Omega_\odot = 2.6 \times 10^{-6}$ rad s⁻¹ or 414 nHz. The viscous time scale at mid-depth $\tau_\nu = L^2/\nu$ is 1250 days for case G1 and is 3640 days for case G5. Additional cases considered other rotation rates at 1.25, 1.5, 1.75 and $6\Omega_\odot$.

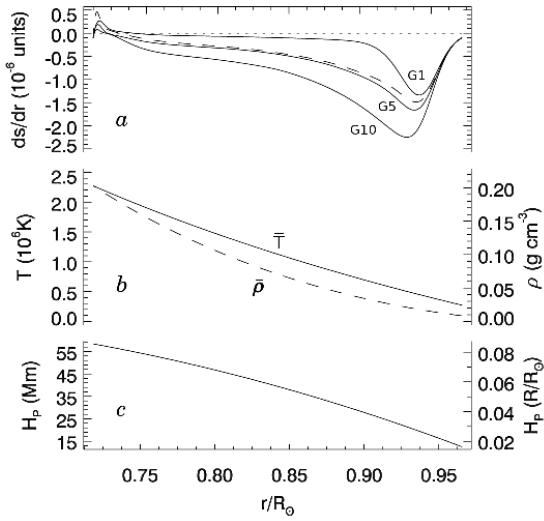


FIG. 1.— Radial variation of mean stellar structure in the ASH models. (a) Entropy gradient ($d\bar{S}/dr$) for cases G1, G5 and G10 (as labeled). At higher rotation rates the entropy gradient becomes steeper throughout the convection zone, even for our most turbulent cases (case G5b, long dashes). (b) Temperature and density (latter ranging from 0.203 to 0.008 g cm⁻³ in the region simulated) for case G1. (c) Pressure scale height H_p (in Mm and fractional solar radii), for case G1, with cases G2-G10 similar in their mean stratification.

Our studies here explore a variety of solar-like stars rotating from 1 to $10\Omega_\odot$ (cases G1-G10). All cases use the same initial stellar structure. We seek here to explore the general effects of rotation on stellar convection rather than the evolution of a particular star, which would require modifications to the stellar structure as the star aged. In surveying the effects of more rapid rotation on global-scale convection, we sought to achieve reasonably high levels of turbulence in the resulting flows. Thus our trajectory through the parameter space of Ω_0, ν , and κ attempts to maintain strong nonlinearity without having increasing the Ω_0 laminarize the convection. As we increased the rotation rate, we simultaneously

decreased the effective eddy diffusivities ν and κ to maintain the supercriticality of the simulated turbulent convection. We note that the critical Rayleigh number for the onset of convection scales with rotation as $\text{Ra}_c \propto \Omega_0^{4/3}$ for Boussinesq convection (e.g., Chandrasekhar 1961; Dormy et al. 2004). Lower diffusivities lead to both longer viscous and thermal diffusion time scales and to flows possessing finer spatial scales. Achieving equilibrated states in these systems requires high resolution simulations carried out over extended periods. We have taken a middle ground between attempting to maintain constant supercriticality (which may require scaling $\nu, \kappa \propto \Omega_0^{-2}$) and keeping resolution requirements reasonable by scaling our diffusivities as $\nu, \kappa \propto \Omega_0^{-2/3}$. However, all of our cases here are still highly supercritical, noting that the critical Rayleigh number for these simulations at $1\Omega_\odot$ is $\text{Ra}_c \sim 1000$ (Gilman & Glatzmaier 1981; Miesch 1998). We have maintained a constant Prandtl number $\text{Pr} = \nu/\kappa = 0.25$ in all of our simulations. The parameters of our models are detailed in Table 1. Our choice of scalings for the eddy diffusivities with rotation rate may have some influence on the nature of the convective patterns and mean flows we achieve. To assess some of the sensitivity the choice of our path through parameter space, we have also sampled a limited range of more turbulent simulations at a few rotation rates (cases G3a, G3b and G5b).

All of the simulations discussed here are at approximately the same level of maturity in their evolution. Case G1 was the progenitor case at $1\Omega_\odot$ and was evolved for some 3000 days after branching away from case AB from Brun & Toomre (2002), which itself has seen about 10000 days of total simulated life. Starting with this case, each subsequent simulation was spun up from the next fastest case (i.e., G3 was spun up from G2) and evolved for over 4000 days, or many hundreds of rotation periods. At this point, all cases appear to be statistically stationary in terms of the angular momentum fluxes and the kinetic energies. We believe that the differential rotation profiles presented are effectively stationary, though there are small fluctuations as determined from short averages over

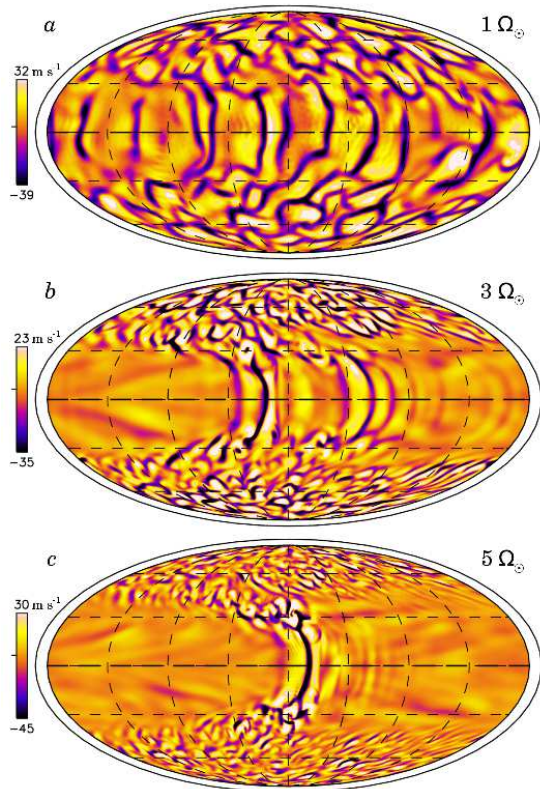


FIG. 2.— Changes in convective patterns with increasing rotation rate for mildly turbulent cases at (a) one, (b) three and (c) five times the solar rate. Shown as snapshots are radial velocities near top of layer in global Mollweide projection, with upflows light and downflows dark. Poles are at top and bottom, and the equatorial region appears at middle, with equator indicated by bold dashed line. Thin dashed lines denote circles of constant latitude or longitude, and the thin surrounding line indicates the location of the stellar surface at R_\odot . A striking pattern of convection localized into nests near the equator emerges as the rotation rate increases.

a few rotation periods. Certain cases (including G5) were evolved for much longer intervals (over 10000 days and more than 2000 rotation periods) to explore the long-term behavior of convective patterns in these rapidly rotating systems. To test that our results are not unduly subject to hysteresis in the system, we explored a branch of cases which were successively spun down from $5 \Omega_\odot$ to $1 \Omega_\odot$. No significant hysteresis was found.

3. CONVECTION IN RAPIDLY ROTATING SUNS

3.1. Early Results of Modulated Convection

In our previous simulations of rapidly rotating suns we found that strongly localized states of convection emerged with more rapid rotation (Brown et al. 2004). A selection of these simulations in Figure 2 present snapshots of radial velocity near the top of the domain in global Mollweide projection, showing the entire spherical surface with minimal distortion. With more rapid rotation, a prominent longitudinal modulation appears in the patterns of equatorial convection. At the higher rotation rates the equatorial convection is confined to one or two nests, with streaming zonal flow filling the regions outside these nests of convection. These nests can persist for intervals spanning many hundreds of rotation periods, often with little change. Two nest states sometimes evolve into single nest states as one nest overtakes another.

The simulations shown in Figure 2 are less turbulent than the cases presented in the rest of this paper, each possessing

Reynolds numbers that are about three-fold smaller near the surface than in our new simulations. In the former models, a large portion of the energy transport in the upper convection zone was carried by unresolved scales of motion. This parametrized SGS flux, represented by κ_0 , dominated transport in the upper 30% of the convection zone, leading to weaker enthalpy transport and weaker resolved convection there. This parametrized flux acts as volume cooling term that removes flux from the regions where it is dominant; the dynamics were influenced by the presence of this cooling layer. The cases presented in this paper have a narrower unresolved flux layer, confined now to the upper 10% of the convection zone, and consequently much more vigorous convection is realized throughout the domain. In these more turbulent cases, the phenomena of localized nests of convection is realized at somewhat higher rotation rates.

3.2. Convective Patterns and Evolution with Rotation

The variation of convective patterns with increasing rotation rate Ω_0 in our more rapidly rotating suns is illustrated in Figure 3. Snapshots of the radial velocity near the top of the domain ($0.95R_\odot$) are shown in Mollweide projection for four cases: G1, G3, G5 and G10. The convection patterns are complex and time dependent, with asymmetries between the upflows and downflows owing to the density stratification: narrow, fast downflow lanes are surrounded by broad, relatively weak upflows.

There is a clear difference in both the scale and structure of convection at high and low latitudes. In the equatorial regions (roughly $\pm 30^\circ$ in latitude), the downflows organize into large structures (loosely called banana cells) aligned with the rotation axis, thus extending in the north-south direction. At high rotation rates this tendency for alignment becomes pronounced, largely in the spirit of the Taylor-Proudman theorem, and the downflow network exhibits little of the east-west branching visible in case G1. These downflow lanes propagate in a prograde sense relative to the bulk rotation rate and do so more rapidly than the differential rotation which they themselves establish. The nests of convection, when they appear at the higher rotation rates, propagate at an intermediate rate as denoted by the heavy dashed contours in Figure 3f-h. We defer discussion of the nature of these nests of convection until later. Individual convective cells persist for about 10 to 30 days.

In the higher latitude regions, the convection cells are more isotropic and the downflow network organizes on smaller scales. Convection in these regions is vigorous and complex, with upflows and their downflow networks in a constant dance. The convective cells have a cusped appearance, with downflows leading upflows as both propagate in a retrograde fashion (most apparent in Figs 3b,c). Strong vortical plumes form in the interstices of the downflow network at both high and low latitudes. In the polar regions above the middle of the convection zone, the sense of vorticity in these downflow plumes is generally cyclonic: counterclockwise in the northern hemisphere and clockwise in the southern. As they descend through the mid-layer their vorticity changes and they become largely anti-cyclonic. In contrast, the polar upflows are anti-cyclonic at all depths.

The latitudinal variation of convection patterns can be in part understood by considering a cylinder tangent to the base of the convection zone and aligned with the rotation axis. Within our geometry, this tangent cylinder intersects the outer boundary at about $\pm 42^\circ$ of latitude. It is well

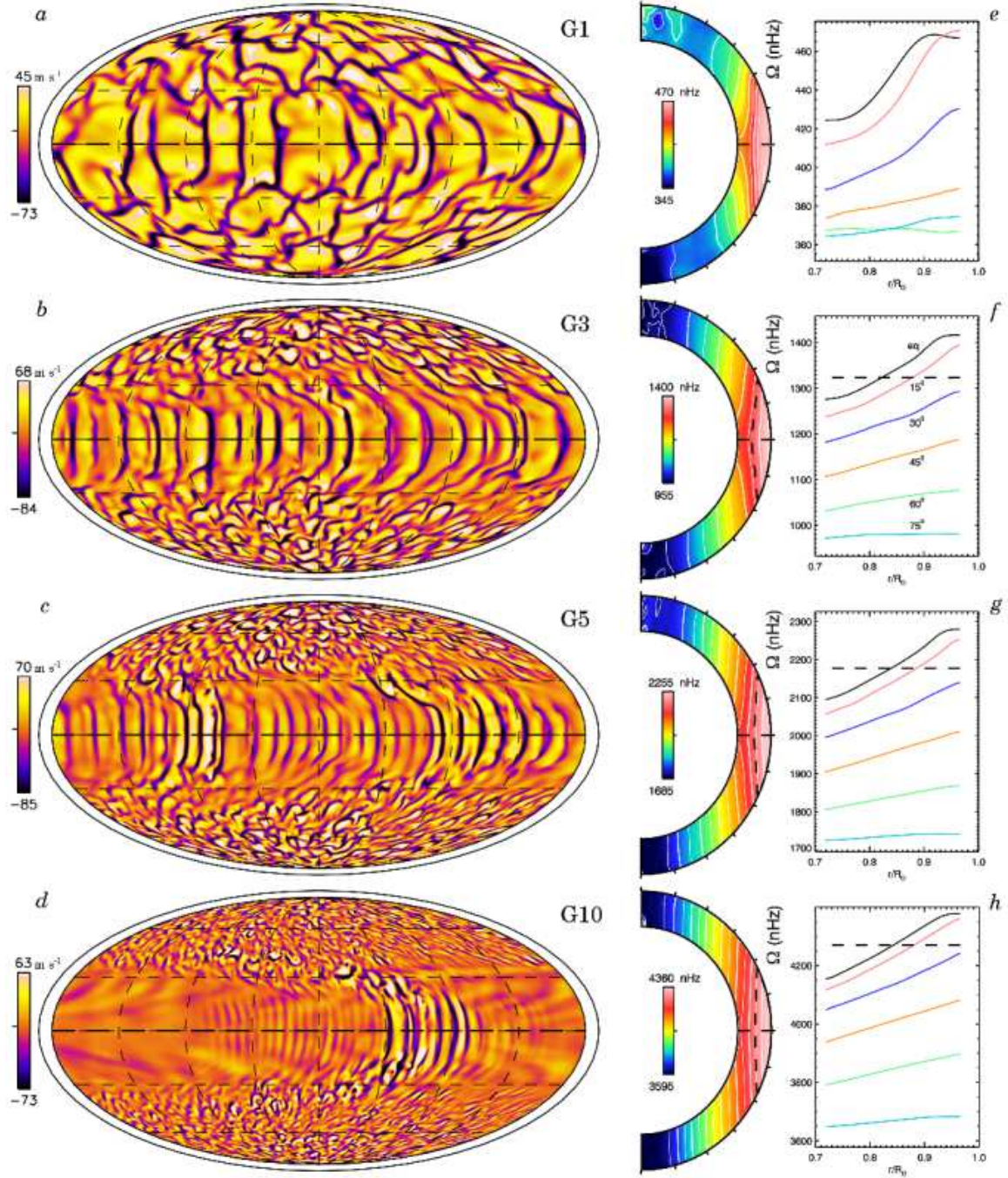


FIG. 3.— Radial velocity patterns in Mollweide projection at $0.95R_{\odot}$ (*left*) and differential rotation profiles (*middle, right*) with increasing rotation rate in (*a,e*) for case G1, (*b,f*) for G3, (*c,g*) for G5, and (*d,h*) for G10. At higher rotation rates the horizontal scale of convective cells shrinks at all latitudes and cells are more strongly aligned with the rotation axis. A striking pattern of modulated convection emerges at low latitudes with faster rotation, consisting of spatially modulated or patchy convection. These active nests of convection are propagating structures which persist for long periods of time. At *middle* are profiles of mean angular velocity Ω with radius and latitude. These differential rotation profiles all involve fast equators (prograde relative to the frame rate Ω_0 , indicated by tickmark on scale) and a monotonic decrease of Ω as the poles are approached. At *right* are radial cuts of the angular velocity at selected latitudes, as labeled. The dark dashed contour denotes the constant propagation rate of the nests where discernible.

known that in a rotating convective shell the flow dynamics are different inside and outside of the tangent cylinder, owing to differences in the connectivity of the flows, the influence of the Coriolis forces and distance from the rotation axis (e.g., Busse 1970). These differences become more evident as the rotation rate, and hence the rotational constraints on the convection, increases. With more rapid rotation the longitudinal extent of the convective cells becomes progressively smaller. Linear theory, in the Boussinesq approximation, predicts that the wavenumber of the most unstable mode scales with rotation as $m \propto \text{Ta}^{1/6} \propto \Omega_0^{1/3} \nu^{-1/3}$ (e.g., Chandrasekhar 1961; Dormy et al. 2004) for polar and equatorial convection. This effect is found in anelastic systems as well (Glatzmaier & Gilman 1981) and in our simulations is evident at both high and low latitudes.

Shown at right in Figures 3e-h are the profiles of differential rotation (as angular velocity Ω) realized in these simulations. These $\Omega(r, \theta)$ profiles are azimuthally and temporally averaged over a period of roughly 200 days. All of our more rapidly rotating solar-like stars exhibit solar-like differential rotation profiles, with prograde (fast) equators and retrograde (slow) poles. Contours of constant angular velocity are aligned nearly on cylinders, influenced by the Taylor-Proudman theorem, though recent simulations of solar convection suggest that this is sensitive to the treatment of the bottom thermal boundary condition (Miesch et al. 2006). As first shown in mean-field models by Rempel (2005) and then in models of global-scale convection by Miesch et al. (2006), introducing a weak latitudinal gradient of entropy at the base of the convection zone, consistent with a thermal wind balance in a tachocline of shear, can serve to rotate the Ω contours toward the more radial alignment deduced from helioseismology without significantly changing either the overall Ω contrast with latitude or the convective patterns. We expect similar behavior here, as briefly explored by Ballot et al. (2007), but have not explored this issue in detail at the higher rotation rates. More rapidly rotating suns may very well also possess tachoclines, but at this stage there is no observational evidence of this. Thus we have simplified these simulations by imposing a constant entropy at the bottom boundary. Our contours of Ω in Figure 3 show some differences between the northern and southern hemispheres, particularly at higher latitudes, and these differences decrease with more rapid rotation. The patterns of convection are not simply symmetric about the equator, and thus the accompanying mean zonal flows can be expected to show some variations between the two hemispheres. Also shown are radial cuts of Ω at six fixed latitudes that make evident the angular velocity contrasts with radius and latitude achieved in these simulations. The absolute contrast in latitude and radius clearly grows with rotation rate, and will be discussed in §4.

A most striking result of our simulations is the emergence of persistent, spatially modulated convection in the equatorial regions at high rotation rates. At these low latitudes, convection becomes modulated in longitude and forms distinct active nests where the convective vigor is enhanced compared to the regions outside. The amplitude of the convective motions and enthalpy transport is larger within these nests, and indeed at the highest rotation rates, convection in the equatorial band is confined entirely to the nests. These nests of convection propagate at a velocity distinct from either the zonal flow of differential rotation or that of the individual cells of convection and persist for very long periods of time (more than 5000 days in

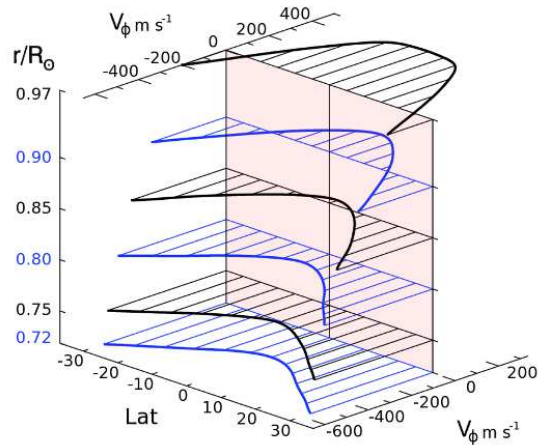


FIG. 4.— Variation of mean zonal velocity $\langle v_\phi \rangle$ with latitude for case G5 sampled at six radial cuts as labeled and shown here relative to the uniform propagation rate of the nests of convection. The nests experience a strong prograde zonal flow (positive) near the top of layer and a prominent retrograde flow within the lower half.

case G5). The nature of these active nests of spatially localized convection will be explored in detail in §7.

Weak modulation in longitude is already evident at low rotation rates. When long time series are considered we have positively identified nests of convection in all simulations rotating at $\Omega_0 \gtrsim 3 \Omega_\odot$. As the rotation rate increases, the modulation level gradually increases; at the highest rotation rates ($\gtrsim 7 \Omega_\odot$) the equatorial convection is almost solely confined to the nests. The convection realized in case G10 (Fig. 3d) is marked by this extreme modulation, with strong upflows and downflows inside the nest and very little convection in the surrounding regions. These most rapidly rotating cases maintain a strong differential rotation profile, even though the equatorial convection occupies only a narrow interval in longitude. The regions outside the nest are filled with fast streaming zonal flows consistent with the differential rotation.

3.3. Radial Connectivity of Convection

The nests of enhanced convection span the convection zone and propagate everywhere at a constant prograde angular velocity relative to the bulk rotation rate of the star. A contour corresponding to this characteristic propagation rate is overplotted on the differential rotation profiles in Figures 3f-h for cases G3, G5 and G10. As is evident from these profiles, the angular velocity associated with the differential rotation exceeds that of the propagation rate of the nests near the surface and is slower than that near the base of the convection zone. The nests of convection therefore live within an environment of substantial zonal shear with radius, as is quantified for case G5 in Figure 4. Here the shearing zonal velocity of differential rotation is plotted in latitude at six radial depths. At all depths there is substantial zonal flow through the nests of convection.

In other studies of solar convection, we have found that strong downflow lanes extend throughout the entire depth of the domain (Miesch et al. 2000; Brun & Toomre 2002; Miesch et al. 2008). In our more rapidly rotating stars, this connectivity with depth changes markedly, as is illustrated for case G5 in Figure 5 showing radial velocities throughout the convection zone. In these rapidly rotating suns, the strong variation of mean zonal flow with radius in the equatorial regions prevents all but the strongest downflows from spanning

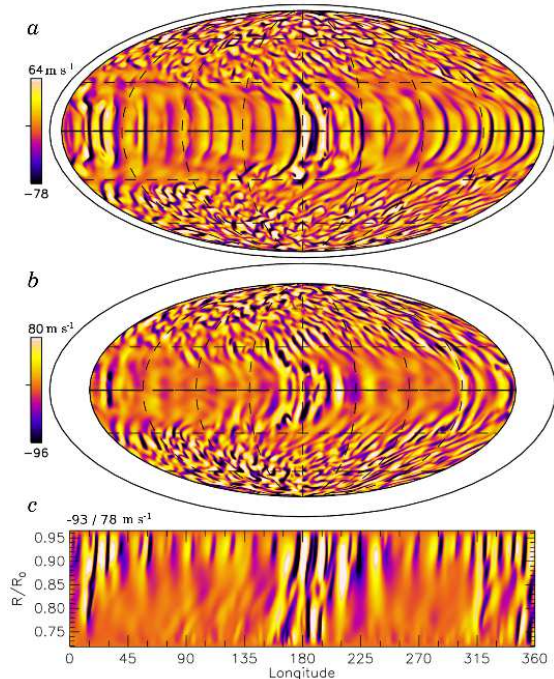


FIG. 5.— Connectivity of radial velocity with depth in case G5, shown at same instant in Mollweide view (a) near top of domain ($0.95R_{\odot}$), (b) at mid depth ($0.85R_{\odot}$), and in (c) for an equatorial cut in longitude over full depth range. Strong plumes span the convection zone in the equatorial regions only within the nest of enhanced convection. The weaker cellular flows outside the nests are confined by shear to the upper reaches.

the convection zone. Within the nest of enhanced convection the plumes are able to traverse the convection zone. Yet in the quieter regions outside, the weaker downflow plumes are truncated by shear before reaching the middle of the convection zone. It is evident (Fig 5c) that the amplitude of convective motions is pronounced at all depths within the nest of active convection.

The downflowing plumes are influenced by the strong radial shear and some break into multiple cells with radius even before the full blown nests of localized convection emerge, as is evident already in our simulation rotating at twice the solar rate (case G2). When the downflow networks only span a portion of the convection zone and experience a limited range of the full density stratification, the importance of compressible effects decreases. This has important consequences for the energetics of the simulations, particularly the radial kinetic energy flux, as will be addressed in §6. In contrast, the downflowing plumes in the polar regions experience much less shear from either the differential rotation or the relatively weak meridional circulations and continue to span the entire convection zone depth.

3.4. Thermal Structuring

In these rapidly rotating suns, the turbulent alignment of convection with the rotation axis leads to a net latitudinal transport of enthalpy, yielding a prominent latitudinal gradient of temperature. The resulting thermal structuring in case G5 is shown in Figure 6, presenting both the mean temperature profile and representative temperature fluctuations in a snapshot near the surface. In the latter, individual convection cells are associated with small fluctuations with amplitudes of a few K. Downflows are generally cool while upflows are relatively warmer. The enhanced enthalpy transport within the active

nests of convection appears as positive temperature fluctuations in the equatorial region.

Evident at high latitudes (Fig. 6c) are broad spatial structures (in addition to small-scale convection) which appear in the temperature fluctuations and are not readily visible in the maps of radial velocity (see Fig. 5 at same instant). These structures are long lived and appear to be a separate phenomena from the nests of convection. The polar patterns propagate in a retrograde sense more rapidly than the differential rotation in which they are embedded, and though streaming wakes from the active nests print weakly into the polar regions, the polar patterns and nests appear to be distinct phenomena. The large-scale polar patterns are not evident in the slowly rotating cases (G1 and G2); in the most rapidly rotating cases this modulation attains a more complicated form than the two-lobed structure shown here.

The zonally-averaged thermal structure (Fig. 6a,b) is quite smooth and is characterized by warm poles and a cool equator, with yet cooler mid-latitudes. In contrast, the mean entropy increases monotonically from equator to pole, due to effects of pressure. All of the more rapidly rotating cases have similar latitudinal thermal profiles, though the temperature difference between equator and pole increases with more rapid rotation, as will be discussed further in §4. In case G5, the latitudinal pole to equator temperature contrast is approximately 100 K throughout the convection zone. These latitudinal variations remain small at all rotation rates in comparison to the spherically symmetric background \bar{T} , which ranges from 2.7×10^5 K near the surface to 2.2×10^6 K near the bottom of the convection zone (as shown in Fig. 1).

4. BUILDING A STRONG DIFFERENTIAL ROTATION

4.1. Thermal Wind Balance

Rapidly rotating systems are constrained by the Taylor-Proudman theorem to have minimal variations in flow dynamics along the direction of the rotation axis. In stratified flows, gradients in density and pressure contribute to baroclinic terms in the vorticity equations (Pedlosky 1982; Zahn 1992) which maintain flows that can break the Taylor-Proudman constraint. In our rapidly rotating suns, convective plumes tilt towards the rotation axis as rotation effects increase. This results in latitudinal as well as radial transport of enthalpy and builds a latitudinal gradient of temperature and entropy. Such gradients arise naturally in a rotating convective system even with uniform thermal boundary conditions. For a nearly adiabatic stratified, rotating, non-magnetized fluid it can be shown that in the limit of small Rossby number and negligible viscous effects the zonal component of the vorticity equations reduces to the well known thermal wind balance (e.g., Brun & Toomre 2002; Miesch et al. 2006):

$$\frac{\partial \widehat{v}_{\phi}}{\partial z} = \frac{g}{2C_{Pr}\Omega_0} \frac{\partial \widehat{S}}{\partial \theta}, \quad (8)$$

where z is directed along the rotation axis and a hat denotes an average in longitude and time. We have further assumed that the turbulent pressure is negligible.

From equation (8) it is clear that departures from rotation constant on cylinders (as observed in the solar interior by helioseismology) can be maintained by a latitudinal gradient of entropy. The left and right hand sides of equation (8) are shown for case G5 in Figure 7. In the bulk of the convection zone, the differential rotation profiles realized in these more rapidly rotating suns are substantially in thermal wind

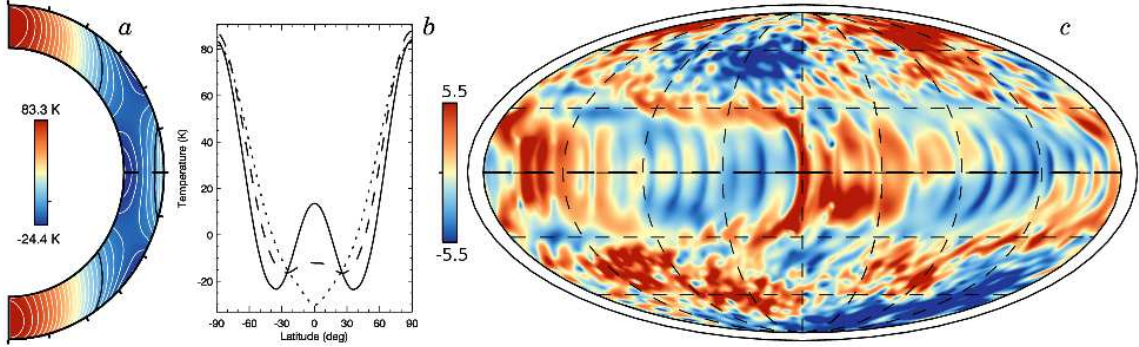


FIG. 6.— Temperature structures within case G5. Mean latitudinal variations in temperature are shown relative to their spherical average \bar{T} in (a) as contours with radius and latitude and (b) as cuts at fixed radii at the top (*solid*, $0.96R_{\odot}$), middle (*dashed*, $0.84R_{\odot}$) and bottom (*dotted*, $0.72R_{\odot}$) of the domain. (c) Temperature fluctuations in a snapshot near top of domain ($0.95R_{\odot}$) relative to the mean structure in (a).

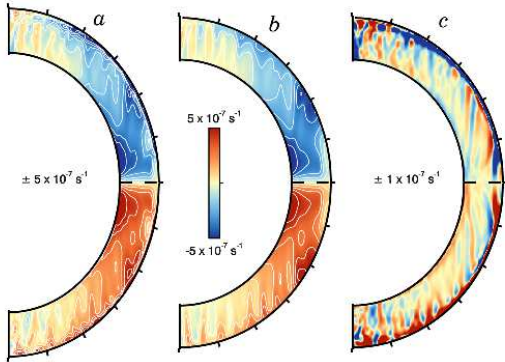


FIG. 7.— Thermal wind balance achieved in case G5. (a) Gradients of \widehat{v}_{ϕ} along the rotation axis, $\partial\widehat{v}_{\phi}/\partial z$, (b) the scaled latitudinal entropy gradient from the right-hand side of eq. (8), and (c) their difference, with contours in the latter rescaled to show the departures near the boundaries. The bulk of the convection zone is in thermal wind balance, but substantial departures arise near the top and bottom of the domain where Reynolds stresses dominate.

balance. Significant departures arise near the inner and outer boundaries (Fig. 7c) where Reynolds stresses and boundary conditions play a dominant role, as was found in earlier simulations of solar convection (Brun & Toomre 2002).

Another striking property of the thermal wind balance is that increasing Ω_0 leads to more cylindrical profiles of \widehat{v}_{ϕ} unless $\partial\widehat{S}/\partial\theta$ also adjusts with the rotation rate. In our more rapidly rotating suns we find that the latitudinal gradients of temperature and entropy increase with more rapid rotation. The growth of $\Delta\widehat{S}$ (difference between the surface value of \widehat{S} at say 60° and the equator) with increasing rotation rate Ω_0 is shown in Figure 8. The latitudinal structure of entropy is always monotonic in these simulations, with lower entropy at the equator and higher entropy at the poles. Convection in these more rapidly rotating systems establishes stronger latitudinal gradients, but not enough in these simulations to maintain the Ω profiles unchanged.

Accompanying the growth of $\Delta\widehat{S}$ is a growth in the latitudinal temperature contrast, as shown by the maximum temperature contrast in latitude near the stellar surface in Figure 8. Typically, the maximal contrast occurs between the poles and latitudes of $\pm 40^\circ$, as seen in Figure 6 for case G5 with a contrast of about 100 K. In the rapidly rotating simulations, the primary flux balance in latitude is between thermal eddy diffusion $\kappa\bar{\rho}\bar{T}\langle\partial S/\partial\theta\rangle$ and convective enthalpy transport $C_p\bar{\rho}\langle v_{\theta}T'\rangle$. Here convective transport moves warm material to the poles as the downflows align more strongly with the rotation axis while eddy diffusion works to erode the gra-

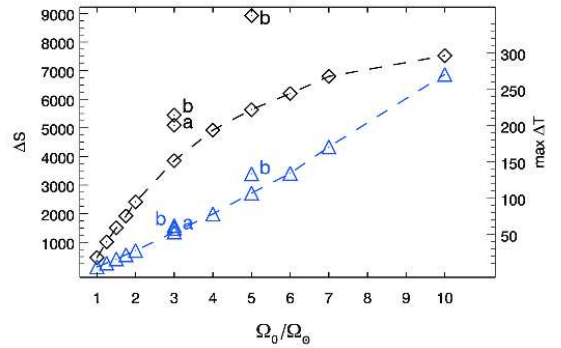


FIG. 8.— Increase with rotation rate in the latitudinal contrast of entropy, $\Delta\widehat{S}$ (plotted as diamonds) between equator and high latitudes at $0.96R_{\odot}$. The more turbulent cases (G3a, G3b and G5b as labeled) have larger entropy contrasts, in keeping with their generally stronger differential rotation. Blue triangles indicate the maximum temperature contrast in latitude at the upper boundary in each simulation.

dient. The meridional circulations appear to play a relatively minor role in maintaining the overall latitudinal entropy contrast.

4.2. Angular Momentum Redistribution

In these simulations of stellar convection, complex couplings between rotation and convection build the profiles of differential rotation and meridional circulation. With stress-free boundary conditions at the top and bottom of the shell there are no net torques and thus the total angular momentum is conserved. Couplings between rotation and convection lead to a global-scale redistribution of angular momentum, resulting in the sustained flows of both differential rotation and meridional circulation. To assess the transport of angular momentum in these systems we follow the approach of Miesch et al. (2008), examining the average radial and latitudinal angular momentum transport as detailed in their equations (10)-(12) (see also Brun & Toomre 2002; Miesch 2005). The angular momentum fluxes from Reynolds stresses (RS), meridional circulations (MS) and viscous diffusion (VD) are

$$\vec{F}^{\text{RS}} = \bar{\rho}r\sin\theta\left(\langle v_r'v_{\phi}'\rangle\vec{r} + \langle v_{\theta}'v_{\phi}'\rangle\vec{\theta}\right), \quad (9)$$

$$\vec{F}^{\text{MC}} = \bar{\rho}\mathcal{L}\left(\langle v_r\rangle\vec{r} + \langle v_{\theta}\rangle\vec{\theta}\right), \quad (10)$$

$$\vec{F}^{\text{VD}} = -\bar{\rho}\nu r^2\sin^2\theta\nabla\Omega, \quad (11)$$

where

$$\mathcal{L} = r\sin\theta\left(\Omega_0 r\sin\theta + \langle v_{\phi}\rangle\right) \quad (12)$$

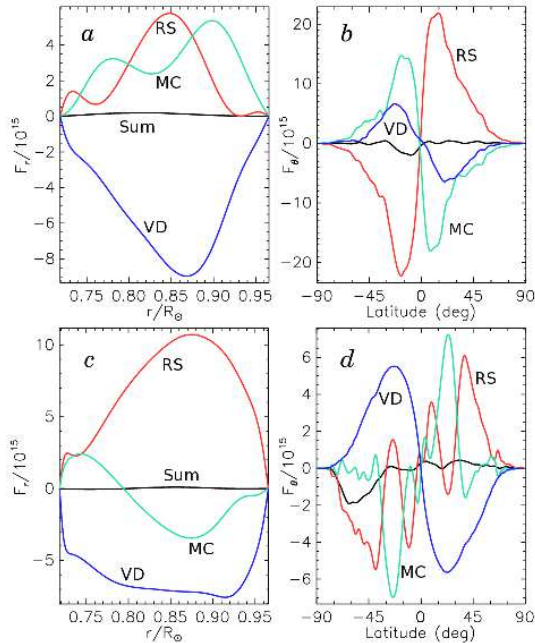


FIG. 9.— Time average of the integrated radial (F_r) and latitudinal (F_θ) angular momentum flux for case G1 (*a, b*) and case G5 (*c, d*). Shown are the fluxes from Reynolds stresses (RS), meridional circulations (MC), viscous diffusion (VD) and their total. Transport by viscous diffusion remains comparable in all cases, while the transport by Reynolds stresses and meridional circulations changes markedly with more rapid rotation.

is the specific angular momentum.

The total radial and latitudinal fluxes of angular momentum are shown for case G1 and G5 in Figure 9. Here we have integrated in co-latitude and radius respectively to deduce the net fluxes through shells at various radii and through cones at various latitudes (c.f., Miesch 2005). The three major contributions arise from Reynolds stresses, meridional circulations and viscous terms. Velocity correlations lead to net angular momentum transport by Reynolds stresses as convective structures develop organized tilts and align partially with the axis of rotation (e.g., Brummell et al. 1998; Brun & Toomre 2002; Miesch et al. 2008). This alignment is particularly prominent in the fast downflow lanes, and becomes stronger as rotation increases.

Turning first to our solar case (G1, Fig. 9*a, b*), we see that in radius the meridional circulations and Reynolds stresses play similar and nearly equal roles in transporting angular momentum outward. The viscous flux meanwhile is negative and transports angular momentum inward, in keeping with the positive radial gradient of the differential rotation profile (eq. 11), and the total flux in radius is nearly zero. The transport in latitude is somewhat different. Here meridional circulations combine with viscous fluxes to transport angular momentum away from the equator and toward the poles (i.e., positive in the southern hemisphere and negative in the northern hemisphere). This tendency is opposed by Reynolds stresses, which continuously accelerate the equatorial regions and dynamically maintain the angular velocity contrast $\Delta\Omega$ in latitude.

The transport of angular momentum in our more rapidly rotating cases are all similar in form and are well represented by case G5 (Fig. 9*c, d*). In these more rapidly rotating stars, the radial balance is dominantly between the Reynolds stresses transporting angular momentum outward and viscous terms

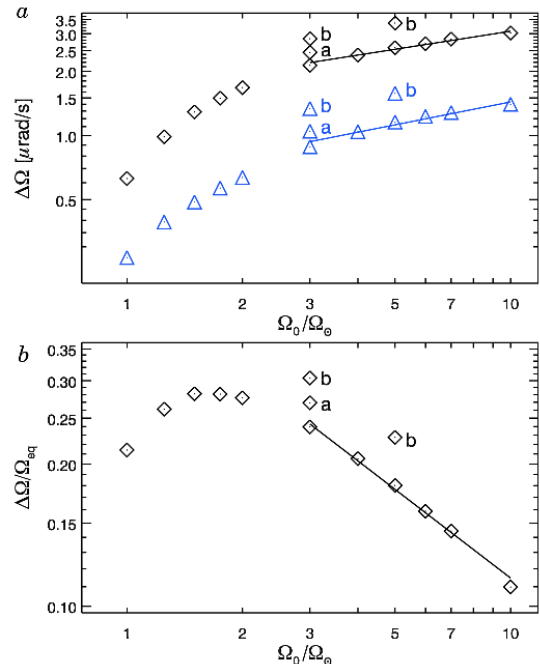


FIG. 10.— (*a*) Angular velocity contrast $\Delta\Omega$ in latitude between equator and 60° (diamonds) and in radius across the shell at the equator (blue triangles). The more rapidly rotating cases appear to follow a power law, which for the latitudinal contrast is $m = 0.3$ and for the radial contrast is $m = 0.4$ (as in eq. 14). (*b*) Relative latitudinal angular velocity contrast $\Delta\Omega/\Omega_{\text{eq}}$, with the shown power law having $n = -0.6$ (as in eq. 13). The scaling may vary with the path in parameter space, as suggested by cases G3a, G3b and G5b.

transporting it inward. The viscous transport is similar in magnitude to that of case G1, though the radial boundary layers are now much narrower. The transport by Reynolds stresses is nearly twice as large, and this likely arises from the strong alignment of convective structures in both polar and equatorial regions. In these stars the weaker meridional circulations become relatively minor and disorganized players in the radial flux balance, moving angular momentum outward in some regions of the shell and inward in others. This opposing behavior between the upper and lower convection zone arises from the meridional circulations breaking into multiple cells in radius.

The balances achieved in the latitudinal transport in case G5 (Fig. 9*d*) are more complex. As the rotation rate has increased, the total viscous transport has remained nearly constant, with the significantly stronger gradients of angular velocity in the differential rotation profiles offset by the lower turbulent diffusivities dictated by our path through parameter space. That these two opposing actions should conspire to produce a nearly constant profile of viscous angular momentum transport is striking and not intuitive. This is particularly apparent when we examine the two other terms in the flux balance. The meridional circulations have reversed their role from our solar-like case G1 and now work with the Reynolds stresses to accelerate the equator and spin down the polar regions. The reduced contribution of the meridional circulations to the total balance arises as the flows become both weaker and multi-celled in radius and latitude. The smaller transport by Reynolds stresses appears to result from the destruction by radial shear of some of the downflow plumes.

4.3. Differential Rotation and Scaling with Rotation

In analyzing our simulation results, it is the differential rotation established by the convection that may yield the most direct contact with observations. Stellar observations across the HR diagram indicate that differential rotation is a common feature in many stars, particularly stars of spectral class F and later. In the sun, differential rotation has been measured throughout the bulk of the convection zone (as reviewed by Thompson et al. 2003), but at present for more distant stars only the surface differential rotation can be inferred. A variety of observational techniques have been employed, ranging from photometric variability studies (e.g., Donahue et al. 1996; Walker et al. 2007), Doppler imaging techniques (e.g., Donati et al. 2003) and Fourier transform methods (e.g., Reiners & Schmitt 2003). Typically, these observations seek to measure the amount of angular velocity contrast at the stellar surface, denoted as $\Delta\Omega_*$, though what is being measured may be somewhat uncertain. Variations in $\Delta\Omega_*$ have been found with both rotation rate and spectral type, however these quantities are correlated and in observations to date it is difficult to disentangle their possible separate effects (Reiners 2006).

Different techniques measure fundamentally different tracers of surface differential rotation, either following variability of Ca emission (photometric), darkening from inferred starspot presence (photometric and Doppler imaging) or rotational broadening of absorption lines of unspotted stars (Fourier transform methods). Each technique also is most applicable in only a limited region of stellar parameter space. As such, overlapping surveys are in short supply. Generally, most observations indicate that the relative shear, $\Delta\Omega_*/\Omega_*$, depends on the stellar rotation rate Ω_* as a power law, though different surveys find different scalings for the differential rotation, expressed as

$$\frac{\Delta\Omega_*}{\Omega_*} \propto \Omega_*^n \quad (13)$$

(e.g., $n = -0.3 \pm 0.1$ in Donahue et al. 1996 and $n = -0.34 \pm 0.26$ in Reiners & Schmitt 2003, but $n = -0.85 \pm 0.10$ in Barnes et al. 2005). Whereas some global models of convection in more rapidly rotating stars have been conducted (e.g., Rüdiger et al. 1998; Küker & Stix 2001; Küker & Rüdiger 2005a,b), these have been largely carried out in 2-D under the simplifying assumptions of mean-field theory.

The amount of latitudinal shear observed at the surface $\Delta\Omega$ is an important quantity both for interpreting stellar observations and for many dynamo theories. Here we define $\Delta\Omega$ more specifically as the difference in angular velocity between the equator and say at 60° latitude, namely

$$\Delta\Omega = \Omega_{\text{eq}} - \Omega_{60} \propto \Omega_0^m. \quad (14)$$

Going to higher latitudes yields comparable behavior. As shown in Figure 10, we find that $\Delta\Omega$ increases with rotation rate in our simulations, with $m = 0.3$ in the most rapidly rotating simulations. The radial shear also increases with more rapid rotation, and at the equator the difference between the mean angular velocity at top and bottom of the shell scales as $m = 0.4$ for the rapid rotators. Because $m < 1$, the relative shear $\Delta\Omega/\Omega_{\text{eq}}$ decreases with rotation rate Ω_0 for the rapid rotators, in nearly a power law fashion for the path through parameter space explored here. The scaling exponent from Equation (13) exhibited by these cases is $n = -0.6$, but this may be influenced by our choice in the scaling of diffusivities with rotation. We are encouraged that our more turbulent cases G3b and G5b, with the same diffusivities at dif-

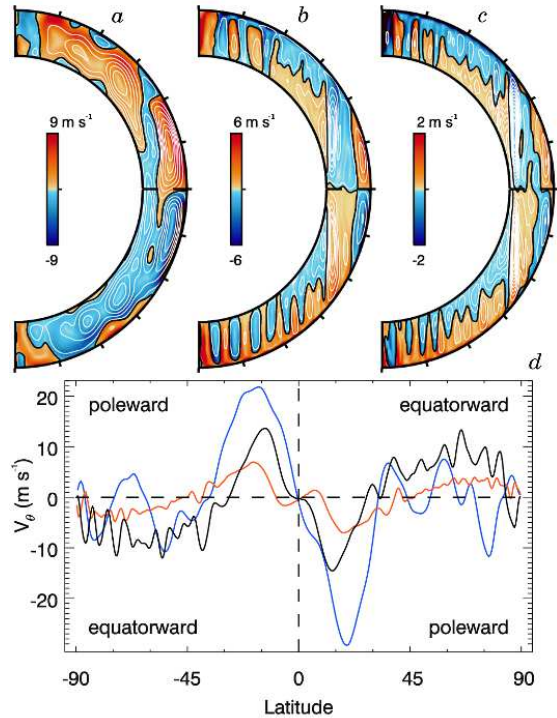


FIG. 11.— Mean meridional circulations with latitude and radius for (a) case G1, (b) case G5 and (c) case G10 with streamlines of mass flux Ψ overlaid. Colors indicate the sense (red counter-clockwise, blue clockwise) and magnitude of the meridional velocity $\langle \vec{v}_m \rangle = \langle v_r \rangle \vec{r} + \langle v_\theta \rangle \vec{\theta}$. With more rapid rotation the meridional circulation cells align strongly with the rotation axis and weaken in amplitude. (d) Amplitude of the mean latitudinal component v_θ at the top of the simulation for case G1 (blue), G5 (black), and G10 (red), with regions of poleward and equatorward flow denoted.

ferent rotation rates, exhibit similar behavior. Our choice of low Prandtl number also has an effect on this scaling (see Ballot et al. 2007). Additionally, different treatments of the SGS unresolved flux, which has the most effect in the upper 10% of the convection zone, can alter the particular scaling law. The early simulations presented in Brown et al. (2004) and shown in Figure 2, which had a much thicker unresolved flux layer, had a scaling of $n = -0.8$ in the rapid rotation limit. We have found that normalizing $\Delta\Omega$ by Ω_0 rather than Ω_{eq} leads to a systematic offset for n of about -0.05 in the inferred scaling law.

5. MERIDIONAL CIRCULATIONS AND SCALING WITH ROTATION

The meridional circulations realized within our simulations are of significance since they can variously transport heat, angular momentum and even magnetic fields between the equator and the poles, though the later are not included in the present simulations. Our time and longitude-averaged meridional circulation patterns are shown in Figure 11 for cases G1, G5 and G10, depicted as streamlines of mass flux Ψ ,

$$r \sin \theta \langle \bar{\rho} v_r \rangle = -\frac{1}{r} \frac{\partial \Psi}{\partial \theta} \quad \text{and} \quad r \sin \theta \langle \bar{\rho} v_\theta \rangle = \frac{\partial \Psi}{\partial r} \quad (15)$$

and averaged here over a period of at least 150 days.

In our more rapidly rotating cases the meridional circulations have broken into several cells strongly aligned with the rotation axis (Fig. 11b,c), particularly in the equatorial regions. Weak connections between the equatorial and polar regions persist at the highest rotation rates studied, with organized flows along the tangent cylinder. These internal

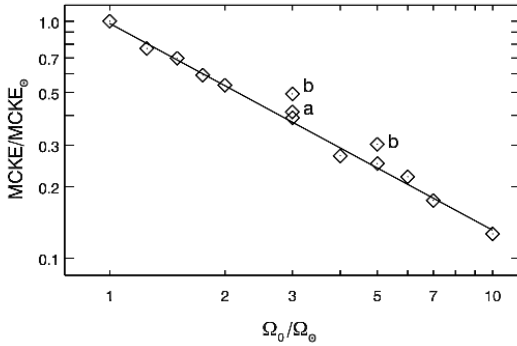


FIG. 12.— Volume-averaged kinetic energy density of the meridional circulations (MCKE) with rotation rate Ω_0 . The MCKE is normalized by that energy in case G1 at the solar rate (2.5×10^4 ergs cm^{-3}). The kinetic energy of these circulations decreases with rotation rate; a power law scaling of $\Omega_0^{-0.9}$ is shown for reference.

flows weaken with more rapid rotation. The meridional circulations are complex and time dependent, with large fluctuations around the statistically-steady states shown here, involving variations comparable to or larger than the mean values themselves. The circulations are driven by small imbalances between relatively large forces and their nature is subtle. The variation of the meridional flows near the surface ($0.96R_\odot$) with rotation rate is shown in Figure 11d. The amplitude of the flows decreases substantially with more rapid rotation. Peak velocities drop from 22 m s^{-1} in case G1 to 14 m s^{-1} in G5 and about 7 m s^{-1} in G10.

The total energy contained in these meridional circulations decreases quickly with more rapid rotation, as shown in Figure 12. This drop in energy is independent of the detailed structure of the convection, showing no change in behavior at the transition to spatially modulated convection. In contrast to the energy contained in convection (CKE) and differential rotation (DRKE), the energy in the meridional circulations (MCKE) is much less sensitive to the level of turbulence in any particular simulation, as indicated by cases G3, G3a and G3b (detailed in Table 2). The meridional circulations remain important to the global-scale dynamics as their gradual redistribution of angular momentum contributes to the large angular velocity gradients in latitude. Yet they are inefficient at transporting heat out of the star and at redistributing thermal material to maintain the latitudinal gradients of temperature and entropy (which correspond to the thermal-wind component of the achieved differential rotation).

This finding is in striking contrast to the assumptions of many Babcock-Leighton dynamos, which often take the meridional velocity to scale as $v_m \propto \Omega$ or $v_m \propto \log \Omega$ (e.g., Charbonneau & Saar 2001; Dikpati et al. 2001). In these models faster meridional circulations lead to shorter dynamo cycles as surface flux is returned more rapidly to the tachocline. Currently, the observational data does not appear good enough to distinguish between the competing models and we will have to await better measurements of the scaling between cycle period and rotation rate and possible observations of the meridional circulations themselves (Rempel 2008). Existing 2-D mean-field models of rapidly rotating stars (Küker & Stix 2001; Rüdiger et al. 1998; Küker & Rüdiger 2005a) also predict an increase of meridional circulation velocities with more rapid rotation. This is in contrast to their decrease in our simulations.

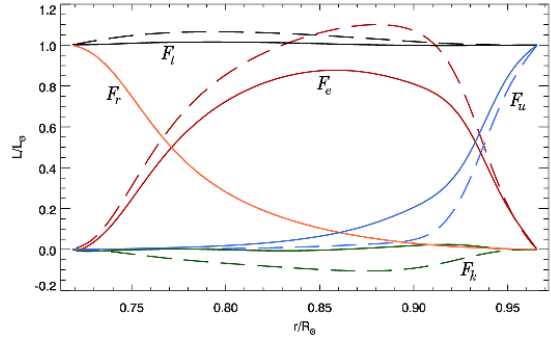


FIG. 13.— Variation of the energy fluxes with radius for cases G1 (*dashed*) and G5 (*solid*). Shown are the radiative luminosity (F_r), convective enthalpy transport (F_e), unresolved flux (F_u), kinetic energy transport (F_k), and the total flux through the simulation (F_t), all normalized by $L_\odot/(4\pi r^2)$. Case G1 has a large positive convective enthalpy flux throughout the domain, with the excess in luminosity largely balanced by an inward flux of kinetic energy. At higher rotation rates (as in G5), the kinetic energy flux is nearly zero throughout the domain. In both cases F_ν is negligible and not shown.

6. ENERGY BALANCES AND FLUX TRANSPORT

Convection is responsible for transporting the stellar flux emerging from the deep interior through the convection zone. In these simulations, the total luminosity $L(r)$ and its components are

$$F_e + F_k + F_r + F_u + F_\nu = \frac{L(r)}{4\pi r^2} = F_t, \quad (16)$$

with

$$F_e = c_p \overline{\rho v_r T'}, \quad F_k = \frac{1}{2} \overline{\rho v_r v^2}, \quad (17)$$

$$F_r = -\kappa_r c_p \overline{\rho} \frac{dT}{dr}, \quad F_u = -\kappa_0 \overline{\rho} \frac{d\overline{S}}{dr}, \quad F_\nu = -\overline{\vec{v} \cdot \vec{D}}|_r, \quad (18)$$

where F_e is the enthalpy transport by convective motions, F_k is the kinetic energy flux, F_r is the transport by radiation, F_u is the unresolved SGS heat flux for parametrized transport by scales of motion below the resolution of our simulation and F_ν is the SGS viscous flux. Figure 13 shows the flux balance with radius achieved in cases G1 and G5, averaged over horizontal surfaces and converted to relative luminosities. In the deepest layers the radiative flux becomes significant as the radiative conductivity steadily increases with depth. By construction it suffices to carry all of the imposed flux through the lower boundary, where the radial velocities and convective flux vanish. A similar role is played near the top of the convection zone by the sub-grid scale transport which yields F_u . The main role of F_u is to transport energy outward through the impenetrable upper boundary where the convective fluxes vanish and the remaining fluxes are small, thereby avoiding the building of strong superadiabatic radial gradients there.

The functional form of $\kappa_0(r)$ is chosen so that the entire stellar luminosity will be transported at the surface of the simulation by F_u . A subtlety of this treatment of the SGS flux lies in $d\overline{S}/dr$. In the more rapidly rotating simulations, we find that convection is less able to establish an adiabatic profile throughout the convection zone. Instead, much of the convection zone remains slightly superadiabatic ($d\overline{S}/dr < 0$). This property is also realized in local-domain simulations of rapidly rotating convection, where more rapid rotation leads to enhanced horizontal mixing through vortex interactions and a resulting decrease in enthalpy transport as vertical velocities and thermal perturbations become more decorrelated (Julien et al. 1996; Brummell et al. 1996). The change of $d\overline{S}/dr$ with rotation rate is shown in Figure 1a for four of

our simulations. Fixing the amplitude and structure of $\kappa_0(r)$ across simulations leads F_u to influence a greater portion of the convection zone at more rapid rotation, as indicated by the slight growth of F_u in case G5. Though this effect becomes stronger as our simulations rotate more rapidly, at no point in these simulations does F_u transport more than 10% of the total luminosity at mid convection zone.

In all these simulations, the strong correlations between radial velocities and temperature fluctuations yield the enthalpy flux F_e , which dominates the energy transport at mid convection zone. Both warm upflows and cool downflows serve to transport flux out of the star, and the two carry comparable amounts of flux to one another in the rapidly rotating simulations. In going to the more rapidly rotating simulations, we find that the average convective enthalpy flux through the polar regions is greater than that through the equator. This is shown in Table 2. In case G1 (at the solar rate) slightly more flux is transported through the equator than the poles, but as the rotation rate increases significantly more flux is transported through the poles than the equator. This latitudinal variation becomes somewhat weaker in our more turbulent cases (G3a, G3b and G5b), but remains present. Interestingly, cases G7 and G10 follow similar trends in their equatorial enthalpy transport, despite the emergence of strong nests of convection at the equator and the suppression of convection in the rest of that region.

In case G1, convection transports slightly more than the solar luminosity. This over luminosity is balanced by an inward transport of kinetic energy, which is primarily due to compressible effects and the transport of v_r^2 within strong downflows that span the convection zone and feel the full density stratification (Hurlburt et al. 1986). In the more rapidly rotating cases, the prominent differential rotation shears apart the convection cells. The downflows have lost much of their coherence and only the strongest downflows within the nests of localized convection survive to span the full convection zone. Individual downflows thus feel less density stratification and compressible effects become less important, leading to a balance in the transport of v_r^2 between the upflows and downflows. Instead, as shown in Table 2 the sense of F_k reverses in the equatorial regions, becoming dominated by the outward transport of v_ϕ^2 . The polar regions remain largely unchanged and the total F_k across spherical surfaces is nearly zero.

Volume-averaged energy densities for a selection of our simulations are shown in Table 2. At the solar rotation rate, convective kinetic energy (with kernel $\frac{1}{2}\bar{\rho}v^2$ and labeled CKE) and the kinetic energy in the average differential rotation ($\frac{1}{2}\bar{\rho}\langle v_\phi \rangle^2$, DRKE) are comparable. As the rotation rate is increased, DRKE grows strongly and convective energy decreases slightly, leading DRKE to dominate the total energy budget. This is true even in our significantly more turbulent solutions. The energy in meridional circulations ($\frac{1}{2}\bar{\rho}\langle v_r \rangle^2 + \langle v_\theta \rangle^2$, MCKE) is always small, and decreases in both magnitude and percentage of the total energy with more rapid rotation.

7. ACTIVE NESTS OF CONVECTION

The emergence of localized nests of convection at higher rotation rates is a striking feature that calls out for an explanation. In many ways, it is quite surprising that convection chooses to be confined to narrow intervals in longitude, but such states have also been realized in a number of other dynamical systems. Generally the appearance of nests is a chal-

lenge to explain in detail, yet the onset of spatially modulated states which may be their precursor is better understood.

7.1. Spatially Localized Convection in Other Settings

The phenomena of spatially localized convection has a rich history, variously appearing in laboratory experiments and numerical simulations. Much interest in confined states of convection was motivated by the discovery of such states in binary fluid convection (e.g., Anderson & Behringer 1990; Kolodner & Glazier 1990; Niemela et al. 1990; Surko et al. 1991), where traveling waves of convection appear via subcritical Hopf bifurcations and near onset are seen to evolve into traveling patches of convection separated by regions of nearly quiescent fluid. From a theoretical perspective, these confined states near onset are accessible to weakly nonlinear theory and considerable progress has been made in understanding their nature (e.g., Riecke 1992; Barten et al. 1995; Batiste & Knobloch 2005; Batiste et al. 2006; Burke & Knobloch 2007). The confined states found in binary convection differ from our active nests of convection in several respects. The most important is that in binary convection there is no net vertical transport of solute. The confined states instead pump solute horizontally and create regions of stable vertical stratification in the quiescent regions. A possibly related phenomena is that of localized states in magnetoconvection, as studied by Blanchflower (1999) and in 3-D by Blanchflower & Weiss (2002). Here single convective cells (called “convectons”) formed in a region of initially uniform strong vertical magnetic field by a process of flux expulsion. Convection within the localized states was strong and was entirely suppressed in surrounding medium. These convectons could contain several convective cells and were generally stationary, though some solutions exhibited time dependent behavior. Recently, progress has been made addressing these systems in approximate 2-D models (Dawes 2007).

Confined states are also realized in other doubly diffusive systems, as in theoretical studies of thermosolutal convection (Knobloch et al. 1986; Deane et al. 1987, 1988; Spina et al. 1998). In the latter studies a variety of traveling convective patches were found, and in these the convective transport of heat and solute was enhanced compared to that in the interpatch regions. In all cases the patches propagated in the same direction as the individual convective cells, though more slowly. Such behavior persisted for long periods of time. These localized states occurred well above the onset of convection, and convection continued in the interpatch regions. There may also be analogues in convection within the Earth’s atmosphere, where deep convection in the tropics tends to be organized on global scales into regions of locally enhanced convection which propagate in a prograde sense. These organized convective structures are called the Madden-Julien Oscillation and appear to have their origin in the coupling of convective motions with equatorially trapped waves (perhaps Rossby or Kelvin waves; see review by Zhang 2005).

The spatially modulated states in our simulations of stellar convection exist at Rayleigh numbers far above the onset of convection. Spatially modulated states in this parameter regime have also been observed in geophysically motivated 3-D Boussinesq simulations of convection within a thick, rotating spherical shell (Grote & Busse 2000; Busse 2002; Busse & Simitev 2005). In these studies, spatially localized states emerged at moderate Rayleigh numbers, involving an equilibrium between the shearing flow of differential rotation destroying convective eddies and the Reynolds stresses in the

TABLE 2
FLUX BALANCES AND ENERGIES

Case	$F_{e,\text{pole}}^a$	$F_{e,\text{eq}}^a$	$F_{k,\text{pole}}^a$	$F_{k,\text{eq}}^a$	CKE ^b	DRKE ^b	MCKE ^b	ΔT_{max}^c
G1	1.014	1.140	-0.118	-0.190	3.28	2.26	0.025	5.50
G2	1.300	0.684	-0.088	0.046	2.64	13.2	0.015	28.0
G3	1.349	0.628	-0.077	0.071	2.40	20.5	0.011	53.5
G4	1.327	0.631	-0.065	0.073	2.21	25.5	0.009	78.5
G5	1.329	0.625	-0.079	0.078	2.11	30.1	0.007	107
G7	1.298	0.581	-0.097	0.080	1.69	38.7	0.005	171
G10	1.236	0.623	-0.093	0.090	1.51	47.1	0.003	271
G3a	1.268	0.655	-0.071	0.068	2.73	27.7	0.012	58.7
G3b	1.101	0.780	-0.065	0.043	3.34	37.9	0.013	62.4
G5b	1.172	0.668	-0.047	0.081	2.44	57.4	0.008	134

^a Average convective enthalpy (F_e) and kinetic energy (F_k) fluxes at mid-layer scaled by the solar flux, shown for polar (latitudes above $\pm 60^\circ$) and equatorial (from $\pm 30^\circ$) regions.

^b Kinetic energy density relative to the rotating coordinate system, for convection (CKE), differential rotation (DRKE) and meridional circulations (MCKE), averaged over the full shell and over ~ 300 days; units are 10^6 erg cm^{-3} .

^c Maximum temperature contrast at $0.96R_\odot$ in K, typically occurring between pole and $\pm 40^\circ$

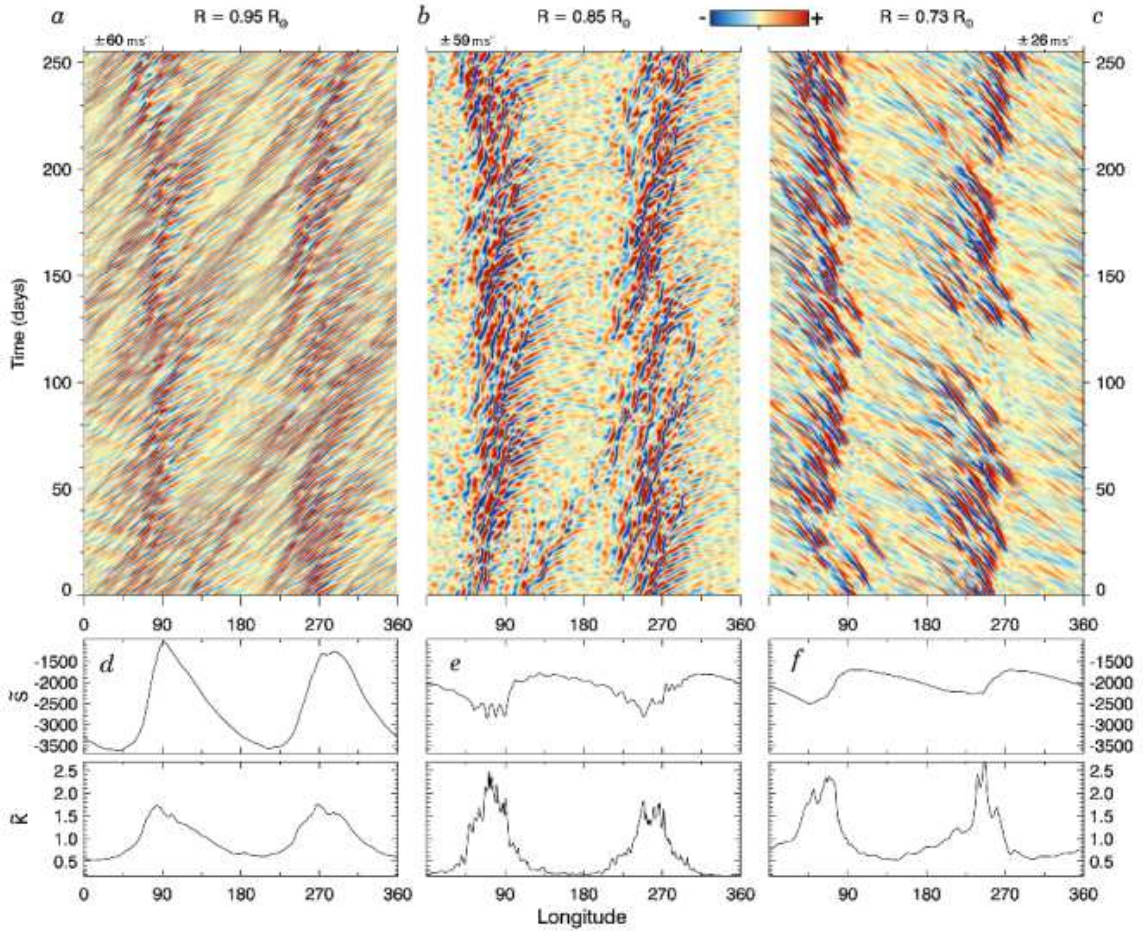


FIG. 14.— Time-longitude map for case G5 of radial velocity v_r , sampled at three depths (*a*) near top, (*b*) middle and (*c*) bottom of layer. These samples are extracted at the equator, using a reference frame tracking the nests and starting from a mature state in the simulation. Two nests are visible, and individual convective cells appear as paired upflows and downflows, which propagate slightly faster than the mean zonal flow that they establish and thus pass through the nests. (*d, e, f*) Time averages with longitude of entropy fluctuations \tilde{S} and convective kinetic energy density \tilde{K} in these samples.

convection driving the differential rotation. These effects led to localized states where convection occupied a limited portion of the domain and the region outside the convective patch was filled with quiescent streaming flow and almost no radial motions. In the quiescent regions the thermal gradients become increasingly unstable until they are advected back into the patch where they help sustain the convective eddies. The patches in these geophysical simulations moved slowly retrograde and persisted up to Rayleigh numbers of about 10^6 . Beyond this point the differential rotation became so strong that no sustained convection was possible. Instead the system began to behave as a relaxation oscillator, with short bursts of convection temporarily building a strong differential rotation which then sheared out the convective eddies. Convective transport remained suppressed until the shear of differential rotation decayed viscously, whereupon a new burst of convection would begin the process anew. In all cases with localized convection, significant oscillations were seen in the kinetic energies of both differential rotation and convection (Grote & Busse 2000).

Similar states have also been realized in anelastic simulations of stellar convection in spherical shells for a rotating younger sun with a much thicker convection zone (Ballot et al. 2006, 2007). The spatially modulated states found there appear in the equatorial convection for models with low Prandtl number ($Pr = 0.25$, as in the models of this paper). Localized states turn into bursty, vacillating convection at large Taylor numbers ($Ta \gtrsim 10^9$), much like those in Grote & Busse (2000). Localized states observed in thick convective shells (with typical aspect ratios $\chi = r_{\text{bot}}/r_{\text{top}} = 0.58$) differ in many important respects from the states we find in our relatively thin shells of convection ($\chi = 0.76$), most notably in their temporal stability, which we will next discuss.

7.2. Properties of the Active Nests

Our active nests of convection appear first as regions of mildly enhanced convective amplitude. As the rotation rate increases, convection in the equatorial regions gradually becomes more localized (as in Fig. 3) and eventually is present only within the active nest. In some of our systems we observe two nests or patches in longitude (such as case G5) and in some only a single nest (as in case G10). Generally, convection at the highest rotation rates possesses only a single nest, and for moderate rotation rates the system can alternate between two-nest states and single-nest states, suggesting that several attractors exist within the phase space.

To study the temporal evolution of our convective patterns in more detail, we employ time-longitude maps as shown in Figure 14. Here radial velocities are sampled at the equator for all longitudes, considering case G5 at three depths (near the top, middle and bottom of the convection zone) and doing so over an interval of 260 days (or about 45 rotation periods). In these maps, structures propagating in a prograde fashion relative to the frame of reference are tilted to the upper-right and patterns propagating in a retrograde sense tilt to the upper-left. To construct these maps we have chosen a frame of reference propagating in a prograde sense relative to the bulk rotation frame ($\Omega_0 = 1.3 \times 10^{-5} \text{ rad s}^{-1}$ or 2070 nHz), with constant relative angular velocity $6.75 \times 10^{-7} \text{ rad s}^{-1}$ (107 nHz, for a total rotation rate of $1.052 \Omega_0$). This corresponds to the propagation rate of the modulated convection pattern, and thus the nests appear stationary in this frame. In the Ω_0 reference frame the nest takes about 108 days to complete one lap

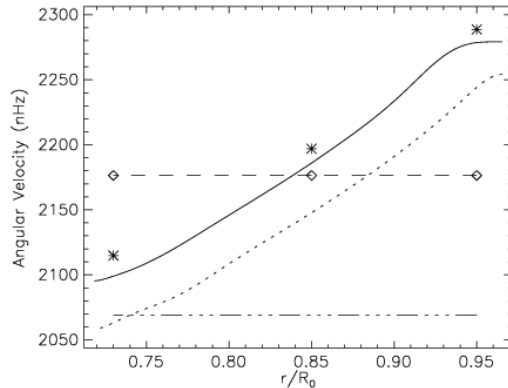


FIG. 15.— Various angular velocities with radius for features in case G5. The mean shearing zonal flow of differential rotation Ω is denoted for all depths at the equator (solid curve) and at $\pm 15^\circ$ latitude (dotted). The propagation rate of the active nests (diamonds) is constant across the entire latitude and radial range where they appear ($\pm 30^\circ$). The average velocity of individual convective cells at the equator (asterisks) is more rapid than the mean zonal flow they establish. Their propagation is faster than the nests near the top and slower near the bottom. The global rotation rate Ω_0 is 2070 nHz (marked).

around the equator, thus for the time interval shown in Figure 14 the nests travel about 870° in longitude and completes about 2.4 circuits around the equator. The active nests of convection can persist for extremely long periods of time. The two nests visible in Figure 14 remain coherent for over 5000 days of simulated time.

Individual convective upflows and downflows appear as streaked red and blue regions respectively. In the upper convection zone ($0.95R_\odot$), the convective cells propagate more rapidly than the nests of convection. Here they overtake the nests from behind (from smaller longitudes) and then slowly swim through at a reduced speed. Within the nests convective cells collide and interact, and the strongest survive to emerge from the front of the nest, where they speed up as they then propagate through the more quiescent region. When this occurs, typically a small wave train comprised of 2 to 3 upflow/downflow pairs escapes, and as they enter the quiescent regions these convective cells speed up to once again outpace the zonal flow. In the lower convection zone ($0.73R_\odot$), the nests propagate more rapidly than the convective cells, and the individual upflows and downflows appear as strong retrograde-directed streaks. Also visible in the lower convection zone are low-amplitude velocity structures of rapid retrograde propagation. They appear to be the weak equatorward extension of the large-scale (retrograde rotating) polar patterns evident in Figure 6. At mid-convection zone ($0.85R_\odot$), nearly all vertical flow is occurring within the nests of active convection, though the strongest cells outside the nest in the upper convection zone manage to weakly print down to this intermediate depth.

The typical angular velocities of the differential rotation, the individual convective cells and the active nests of convection are shown in Figure 15 for case G5 and detailed for several cases in Table 3. The nests of convection propagate at a constant angular velocity at all depths in the convection zone and over the entire range of latitudes ($\pm 30^\circ$) where they are present. In contrast, the angular velocity Ω of the differential rotation varies substantially with radius and latitude. At all depths, the individual convective cells propagate more rapidly than the zonal flow of differential rotation which they drive. Because the nests of convection propagate at an intermediate

TABLE 3
ANGULAR VELOCITIES OF VARIOUS STRUCTURES

Case	Ω_0	Ω_{nest}	$\Omega_{\text{eq,top}}$	$\Omega_{\text{eq,bot}}$	$\Omega_{c,\text{top}}$	$\Omega_{c,\text{bot}}$
G1	2.60	—	0.341	0.060	0.535	0.180
G3	7.80	0.511	1.094	0.220	1.176	0.330
G5	13.00	0.675	1.319	0.197	1.381	0.288
G10	26.00	0.830	1.497	0.140	1.623	0.280
G3a	7.80	0.690	1.295	0.265	1.421	0.373
G3b	13.00	0.670	1.555	0.250	1.590	0.413
G5b	13.00	0.750	1.778	0.246	1.800	0.430

NOTE. — All angular velocities in $\mu\text{rad s}^{-1}$ and, except for the frame rate Ω_0 , are given relative to Ω_0 . The differential rotation at the equator Ω_{eq} is measured at $0.95R_\odot$ (*top*) and $0.73R_\odot$ (*bot*). The mean propagation rate of individual convective structures Ω_c is measured at the same depths in time-longitude maps of v_r and has a typical variance of $\pm 0.04 \mu\text{rad s}^{-1}$.

prograde rate, they experience a head-wind from the differential rotation in the deep convection zone and a tail-wind near the surface. Despite this strong radial shear, the nests remain coherent across the entire convection zone for long periods compared with either the lifetime of individual convective cells (10-30 days), the rotation period of the star (5 days) or typical thermal and viscous diffusion times ($\tau_\kappa = 910$ days, $\tau_\nu = 3640$ days, both at mid-depth). The time for the differential rotation to lap the nests at the equator is about 112 days near the surface and 143 days at the bottom of the shell.

At the higher rotation rates, single stable nests of convection dominate the equatorial region. Time-longitude maps are shown in Figure 16 for the equatorial radial velocity at two depths in case G10, our most rapidly rotating simulation. Within the nest, convection remains vigorous, with the strongest downflow networks still spanning the entire depth of the convection zone. This nest again propagates in a prograde sense relative to Ω_0 , with constant relative angular velocity $8.3 \times 10^{-7} \text{ rad s}^{-1}$ (132 nHz, for a total rotation rate of $1.032 \Omega_0$). Over the interval shown the nest completes almost 3 circuits of the equator relative to the Ω_0 reference frame. Individual convective cells continue to swim through the nest, moving more rapidly near the surface and more slowly in the deep convection zone. The very strong radial shear prevents all but the strongest of downflows from spanning the full convection zone. In the region outside the nest, convection is strongly suppressed and the main features are the weak flows associated with the retrograde propagating polar pattern. In the upper convection zone, occasional weak convective disturbances appear upstream of the nest. As these fluctuations enter the nest they grow in amplitude.

Our nests of active convection may owe their existence to a competition between the shearing action of differential rotation acting on the individual convective eddies and Reynolds stresses within the convection helping to maintain the strong zonal flows. Unlike the systems studied by Grote & Busse (2000) and Ballot et al. (2007), our patchy convection is not accompanied by relaxation oscillation behavior or large exchanges between the kinetic energy in convection and in the differential rotation. Rather, our nests are not bursty in time and instead persist for long periods in quasi-steady states. This is true even for our most rapidly rotating case considered here (G10) and at much higher turbulent driving (G5b), though these simulations exist at Taylor numbers below the threshold suggested by Ballot et al. (2007) ($\text{Ta} \gtrsim 10^9$). Coupling between equatorially trapped waves and convection may

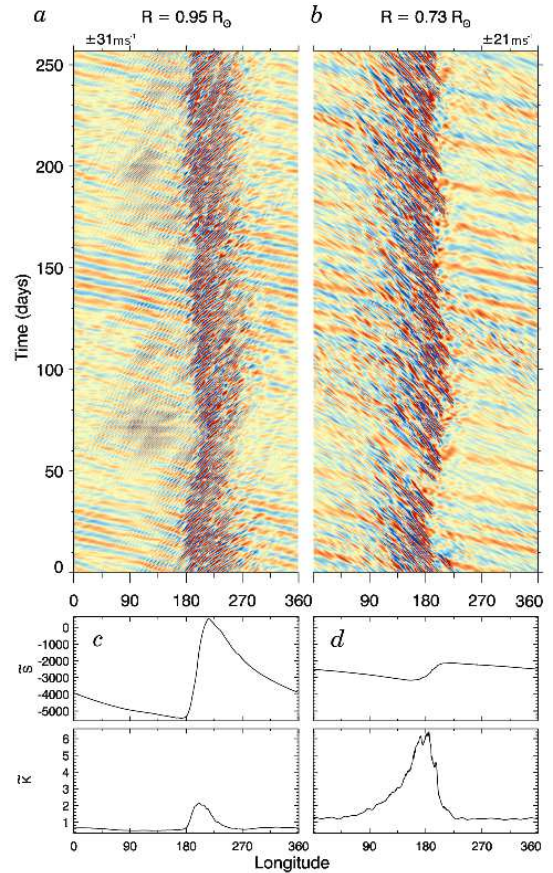


FIG. 16.— As in Fig. 14, time-longitude map for case G10 of radial velocity (*a*) near top and (*b*) near bottom of layer. Here a single nest is realized, with individual convective cells almost entirely confined to the nest, though they continue to propagate within it. (*c*, *d*) Time averages \bar{S} and \bar{K} constructed in the same reference frame.

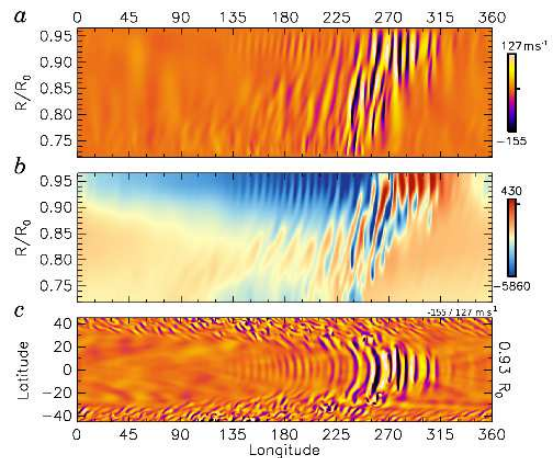


FIG. 17.— Snapshot of nest structure in case G10, at relative day 221 of Fig. 16. (*a*) Radial velocities in an equatorial cut shown for all longitudes and radii. (*b*) Companion entropy fluctuations S about their spherical means \bar{S} (in cgs units), with high entropy fluid in red tones. (*c*) Radial velocity in the equatorial region shown near the top of layer.

also have a role, but the contribution of this coupling to spatial localization has been difficult to elucidate.

7.3. Detailed Structure of an Active Nest of Convection

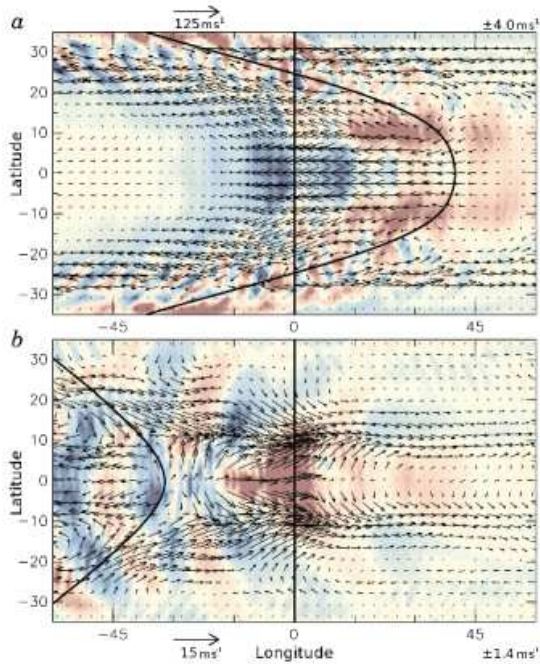


FIG. 18.— Mean circulations associated with the nest in case G10. (a) Time averaged radial (colors) and horizontal flows (arrows) near the top and (b) near the bottom of the shell, in a reference frame tracking the nest. The strong zonal flow of differential rotation has been subtracted at each latitude and is shown by the solid curves (both scaled by 125 m s^{-1} arrow length, with zero velocity relative to the nest indicated by the vertical line). Within the nest strong eddy currents partially decelerate the flow, while outside the streaming mean zonal flow dominates.

We focus here on the structure of the nests so evident in Figures 14 and 16 for cases G5 and G10, but devote particular attention to the single nest realized in the latter as a representative case. The active nests extend throughout the depth of the convection zone. This is illustrated most clearly in Figure 17a, showing the vertical profile of radial velocities with longitude in a cut at the equator. Convection is broken into multiple cells, one set above $0.9R_{\odot}$ and another below $0.8R_{\odot}$. Only within the nest do strong downflows span the convection zone. The nest is embedded in a region of strong latitudinal and radial zonal shear (as shown by the tilted nature of its structure), yet the pattern propagates at a constant angular velocity at all depths and latitudes. At the surface and near the equator the nest propagates more slowly than the zonal wind, whereas at the base of the convection zone it propagates more rapidly. Individual convective structures swim still more rapidly and both enter and exit the region of enhanced convection. As such, the nest experiences a strong retrograde flow at the base and a strong prograde flow near the surface.

The thermal structure of the nests is revealed by their entropy fluctuations, as shown in Figure 17b. In the upper convection zone, the mean zonal flow advects low entropy fluid into the nests from the left side. This fluid is then swept away by intermittent downflows and replaced by higher entropy fluid from below. In the lower convection zone, higher entropy fluid is swept into the nest from the right and lower entropy exits to the left. At mid convection zone, regions outside the nest remain convectively unstable, but only weak radial motions are driven here.

The mean longitudinal structure of the nests can be assessed by forming temporal averages of various properties in a frame

co-rotating with the nests of convection (these averages denoted by a tilde). This is done at the equator for entropy \tilde{S} and convective kinetic energy density \tilde{K} (with same form as CKE) for case G5 in Figure 14d–f and for case G10 in Figure 16c,d. There are distinctive differences between the leading (to the right) and trailing (to the left) portions of the profiles, with \tilde{S} showing a gradual rise and steeper drop in going to decreasing longitudes (from right to left). The envelope of \tilde{S} is largely similar in form at the top and bottom of the convection zone. In contrast \tilde{K} , which traces the fluctuating velocities of convection, changes form with depth, being skewed in the direction of the mean zonal flow. At the top of the convection zone this sense of skew is toward the right, and at the bottom it is toward the left.

These nests must have gradual circulations associated with them, though these are a challenge to discern as they are much weaker than the strong mean zonal flows. We can get some sense of them by averaging the vertical and horizontal flows in the surroundings of a nest while tracking it over long time intervals. Shown in Figure 18 are the slow circulations associated with the nest in case G10 near the top and bottom of the convection zone. These flows have been averaged over a period of 615 days starting at the beginning of the interval shown in Figure 16. The flows suggest a systematic zonal circulation from fore to aft in the upper convection zone and toward higher latitudes and diverging from the nest at depth, though to achieve this we have subtracted the fast mean zonal flow which varies with latitude as shown. The mean upflows and downflows in the nest are quite weak, with amplitudes of a few m s^{-1} , as compared with the convection which can have peak velocities of a few hundred m s^{-1} . Test particles released in the flow would not simply circulate according to these mean circulations and would be instead swept along by the strong mean zonal flow and of course by the vigorous convection cells that propagate through the nest. Some test particles would encounter strong downflows and would be swept down through the nest to the bottom of the convection zone while others would likely be carried horizontally out the nest and remain at a similar depth. Yet Figure 18 indicates that a weak large-scale circulation is realized, and this may serve to slowly pump fluid through the system. These mean circulatory flows may also serve to inform analytic models of such nests of convection.

8. CONCLUSION

When stars like our sun are young they rotate much more rapidly than the present sun. In these stars rotation must strongly influence the convective motions and may lead to stronger global-scale dynamo action. We have explored here the effects of more rapid rotation on global-scale convection in simulations of stars like our sun. The mean zonal flows of differential rotation become much stronger with more rapid rotation, scaling as $\Delta\Omega \propto \Omega_0^{0.3}$ or as $\Delta\Omega/\Omega_{\text{eq}} \propto \Omega_0^{-0.6}$. In striking contrast, the meridional circulations become much weaker with more rapid rotation, and the energy contained in them drops approximately as $\Omega_0^{-0.9}$. Accompanying the growing differential rotation is a significant latitudinal temperature contrast, with amplitudes of 100 K or higher in the most rapidly rotating cases. The maximum temperature contrast near the surface occurs between the hot poles and the cool mid latitudes at about $\pm 40^\circ$. If this latitudinal temperature contrast prints through the vigorous convection at the stellar surface, it may appear as an observable latitudinal variation

in intensity. The thermal contrast would presumably persist for long periods compared to stellar activity, offering a way to disentangle this intensity signature from that caused by spots of magnetism at the stellar poles.

These simulations are entirely hydrodynamic and this provides a major caveat to our findings on the scaling of differential rotation and latitudinal temperature contrast with rotation rate Ω_0 . Prior MHD simulations of stellar convection have demonstrated that in some parameter regimes strong dynamo-generated magnetic fields can react back strongly on the differential rotation, acting to lessen angular velocity contrasts or largely eliminate them (e.g., Brun et al. 2005; Featherstone et al. 2007; Browning 2008). It is unclear whether the scaling trends identified here for differential rotation as a function of Ω_0 will survive in the presence of dynamo action and magnetic fields. Likewise, magnetic fields may lessen the strong temperature contrasts realized here, doing so through their feedback on the convective flows and energy transport. We expect that the weaker meridional circulations may be less affected by magnetic feedbacks, and thus the prediction that meridional circulations lessen in energy and amplitude with more rapid rotation may be of greater significance though harder to confirm observationally. Weaker meridional circulations in more rapidly rotating stars will have a strong impact on many theories of stellar dynamo action, including the Babcock-Leighton flux-transport model favored for solar-type stars. We have begun simulations to explore the dynamo action realized at various rotation rates, and its impact upon the flows described here. Preliminary results appear in Brown et al. (2007) and more detailed results will be forthcoming shortly.

A striking feature of these simulations is the emergence of a pattern of strongly modulated convection in the equatorial regions. These nests of active convection are regions of enhanced convective vigor and transport which propagate at rates distinct from either the mean zonal flows of differential rotation or the individual convective cells. In the most rapidly rotating systems, such as case G10, convection at the equator is entirely dominated by motions inside the nest with only very weak radial motions present in the regions outside the nest. Though their impact on the convection is most obvious in the rapidly rotating limit, we find some evidence for weak modulation even in our more slowly rotating cases.

All of our simulations stop short of the turbulent stellar surface, and it is thus difficult to estimate how these nests of active convection may affect stellar observations in detail. The convective velocities associated with the nests are small com-

pared to the nearly supersonic flows in stellar granulation, and in the sun such global-scale convective structures have evaded direct detection despite intensive searches throughout the near-surface layers by helioseismology. The extremely localized nests found in our most rapidly rotating cases may however influence the thermal stratification and thus convective vigor in the near surface regions, as most of the flux at the equator is transported through a narrow range of longitudes. These nests may act as traveling hot spots with enhanced convection even in the surface layers where the higher emerging flux escapes the system.

These spatially localized states of convection may also have some bearing on the active longitudes of magnetic activity observed in the sun, if the enhanced pummeling of the tachocline by the convection within the nest preferentially destabilizes magnetic structures within the tachocline that then rise to the surface. Initial dynamo simulations indicate that nests of convection can coexist with magnetism in portions of parameter space. Thus their strongest signature is likely to emerge in magnetic stars, where magnetic fields threading the bulk of the convection zone may be concentrated in the nests and mimic giant, propagating starspots which survive for very long epochs in time. If the nests lead to active longitudes of enhanced magnetic activity in rapidly rotating stars, we might expect these long-lived magnetic structures to propagate at a rate different from the stellar rotation rate as measured at the surface or from the stellar differential rotation.

We recognize that our simulations remain separated by many orders of magnitude from the parameter space of real stellar convection. As such, we must be cautious with our interpretations of the overall dynamics. However, we have found that these nests of convection are a robust feature over a range of parameters and that they are able to persist as entities for as long as we could pursue their modelling. Thus one should be prepared to consider the possibility of their presence also in real stellar convection zones, where they may appear as long-lived propagating features.

This research is supported by NASA through Heliophysics Theory Program grants NNG05G124G and NNX08AI57G, with additional support for Brown through the NASA GSRP program by award number NNG05GN08H. Browning was supported by a NSF Astronomy and Astrophysics postdoctoral fellowship AST 05-02413. The simulations were carried out with NSF PACI support of PSC, SDSC and NCSA, and by NASA support at Project Columbia.

REFERENCES

- Anderson, K.E., & Behringer, R.P. 1990, *Phys. Lett. A*, 145, 323
 Ballot, J., Brun, A. S., & Turck-Chièze, S. 2006, in *Beyond the Spherical Sun: A New Era of Helio- and Asteroseismology*, ed. K. Fletcher, & M. Thompson, (ESA SP-624; Noordwijk: ESA), 108.1
 Ballot, J., Brun, A.S., & Turck-Chièze, S. 2007, *ApJ*, 669, 1190
 Barnes, J.R., Cameron, A.C., Donati, J.-F., James, D.J., Marsden, S.C., & Petit, P. 2005, *MNRAS*, 357, L1
 Barten, W., Lücke, M., Kamps, M., & Schmitz, R. 1995, *Phys. Rev. E*, 51, 5662
 Batiste, O., & Knobloch, E. 2005, *Phys. Rev. Lett.*, 95, 244501
 Batiste, O., Knobloch, E., Alonso, A., & Mercader, I. 2006, *J. Fluid Mech.*, 560, 149
 Blanchflower, S. 1999, *Phys. Lett. A*, 261, 74
 Blanchflower, S., & Weiss, N.O. 2002, *Phys. Lett. A*, 294, 297
 Brown, B.P., Browning, M.K., Brun, A.S., Miesch, M.S., Nelson, N.J., & Toomre, J. 2007, in *Unsolved Problems in Stellar Physics*, ed. R.J. Stancliffe et al., *Amer. Inst. Phys.*, CP-948, 271.
 Brown, B.P., Browning, M.K., Brun, A.S., & Toomre, J. 2004, in *Helio- and Asteroseismology: Towards a Golden Future*, ed. D. Damesy, (ESA SP-559; Noordwijk: ESA), 341
 Browning, M.K. 2008, *ApJ*, 676, 1262
 Browning, M.K., Brun, A.S., & Toomre, J. 2004, *ApJ*, 601, 512
 Browning, M.K., Miesch, M.S., Brun, A.S., & Toomre, J. 2006, *ApJ*, 648, L157
 Brummell, N.H., Hurlburt, N.E., & Toomre, J. 1996, *ApJ*, 473, 494
 —. 1998, *ApJ*, 493, 955
 Brun, A.S., Antia, H.M., Chitre, S.M., & Zahn, J.-P. 2002, *A&A*, 391, 725
 Brun, A.S., Browning, M.K., & Toomre, J. 2005, *ApJ*, 629, 461
 Brun, A.S., Miesch, M.S., & Toomre, J. 2004, *ApJ*, 614, 1073
 Brun, A.S., & Toomre, J. 2002, *ApJ*, 570, 865
 Burke, J., & Knobloch, E. 2007, *Phys. Lett. A*, 360, 681
 Busse, F.H. 1970, *J. Fluid Mech.*, 44, 441
 —. 2002, *Phys. Fluids*, 14, 1301
 Busse, F.H., & Simitev, R. 2005, *Astron. Nachr.*, 326, 231

- Chandrasekhar, S. 1961, *Hydrodynamic and Hydromagnetic Stability* (Oxford: Clarendon)
- Charbonneau, P. 2005, *Living Rev. Sol. Phys.*, 2, 2, <http://www.livingreviews.org/lrsp-2005-2>
- Charbonneau, P., & Saar, S.H. 2001, in *Magnetic Fields Across the Hertzsprung-Russell Diagram*, ed. G. Mathys, S.K. Solanki, & D.T. Wickramasinghe, ASP Conf. Ser., Vol. 248, 189
- Clune, T.L., Elliott, J.R., Glatzmaier, G.A., Miesch, M.S., & Toomre, J. 1999, *Parallel Comp.*, 25, 361
- Dawes, J.H.P. 2007, *J. Fluid Mech.*, 570, 385
- Deane, A.E., Toomre, J., & Knobloch, E. 1987, *Phys. Rev. A*, 36, 2862
- . 1988, *Phys. Rev. A*, 37, 1817
- Dikpati, M., Saar, S.H., Brummell, N., & Charbonneau, P. 2001, in *Magnetic Fields Across the Hertzsprung-Russell Diagram*, eds. G. Mathys, S.K. Solanki, & D.T. Wickramasinghe, ASP Conf. Ser., Vol. 248, 235
- Donahue, R.A., Saar, S.H., & Baliunas, S.L. 1996, *ApJ*, 466, 384
- Donati, J.-F., Cameron, A.C., Semel, M., Hussain, G.A.J., Petit, P., Carter, B.D., Marsden, S.C., Mengel, M., López Ariste, A., Jeffers, S.V., & Rees, D.E. 2003, *MNRAS*, 345, 1145
- Dormy, E., Soward, A.M., Jones, C.A., Jault, D., & Cardin, P. 2004, *J. Fluid Mech.*, 501, 43
- Featherstone, N., Browning, M.K., Brun, A.S., & Toomre, J. 2007, *Astron. Nachr.*, 328, 1126
- Gilman, P. A. 1975, *J. Atmos. Sci.*, 32, 1331
- . 1977, *Geophys. Astrophys. Fluid Dynam.*, 8, 93
- . 1979, *ApJ*, 231, 284
- Gilman, P.A., & Glatzmaier, G.A. 1981, *ApJS*, 45, 335
- Glatzmaier, G.A., & Gilman, P.A. 1981, *ApJS*, 45, 351
- Grote, E., & Busse, F.H. 2000, *Fluid Dynam. Res.*, 28, 349
- Hurlburt, N.E., Toomre, J., & Massaguer, J.M. 1986, *ApJ*, 311, 563
- Julien, K., Legg, S., McWilliams, J., & Werne, J. 1996, *J. Fluid Mech.*, 322, 243
- Knobloch, E., Moore, D.R., Toomre, J., & Weiss, N.O. 1986, *J. Fluid Mech.*, 166, 409
- Kolodner, P., & Glazier, J.A. 1990, *Phys. Rev. A*, 42, 7504
- Küker, M., & Rüdiger, G. 2005a, *A&A*, 433, 1023
- . 2005b, *Astron. Nachr.*, 326, 265
- Küker, M., & Stix, M. 2001, *A&A*, 366, 668
- Miesch, M.S. 1998, Ph.D. thesis, University of Colorado, Boulder
- . 2005, *Living Rev. Sol. Phys.*, 2, 1, <http://www.livingreviews.org/lrsp-2005-1>
- Miesch, M.S., Brun, A.S., DeRosa, M.L., & Toomre, J. 2008, *ApJ*, 673, 557
- Miesch, M.S., Brun, A.S., & Toomre, J. 2006, *ApJ*, 641, 618
- Miesch, M. S., Elliott, J.R., Toomre, J., Clune, T.L., Glatzmaier, G.A., & Gilman, P.A. 2000, *ApJ*, 532, 593
- Niemela, J.J., Ahlers, G., & Cannell, D.S. 1990, *Phys. Rev. Lett.*, 64, 1365
- Noyes, R.W., Hartmann, L.W., Baliunas, S.L., Duncan, D.K., & Vaughan, A.H. 1984, *ApJ*, 279, 763
- Patten, B.M., & Simon, T. 1996, *ApJS*, 106, 489
- Pedlosky, J. 1982, *Geophysical Fluid Dynamics* (New York: Springer-Verlag)
- Reiners, A. 2006, *A&A*, 446, 267
- Reiners, A., & Schmitt, J.H.M.M. 2003, *A&A*, 398, 647
- Rempel, M. 2005, *ApJ*, 622, 1320
- . 2008, in *Helioseismology, Asteroseismology and MHD Connections*, J. Physics Conf. Ser. (IoP), in press
- Riecke, H. 1992, *Phys. Rev. Lett.*, 68, 301
- Rüdiger, G., von Rekowski, B., Donahue, R.A., & Baliunas, S.L. 1998, *ApJ*, 494, 691
- Spina, A., Toomre, J., & Knobloch, E. 1998, *Phys. Rev. E*, 57, 524
- Surko, C.M., Ohlsen, D.R., Yamamoto, S.Y., & Kolodner, P. 1991, *Phys. Rev. A*, 43, 7101
- Thompson, M. J., Christensen-Dalsgaard, J., Miesch, M.S., & Toomre, J. 2003, *ARA&A*, 41, 599
- Walker, G.A.H., Croll, B., Kuschnig, R., Walker, A., Rucinski, S.M., Matthews, J.M., Guenther, D.B., Moffat, A.F.J., Sasselov, D., & Weiss, W.W. 2007, *ApJ*, 659, 1611
- Zahn, J.-P. 1992, *A&A*, 265, 115
- Zhang, C. 2005, *Rev. Geophys.*, 43, G2003